



**AFRL-AFOSR-VA-TR-2016-0308**

---

Hierarchically-Driven Approach for Quantifying Fatigue Crack Initiation  
and Short Crack Growth Behavior in Aerospace Materials

**Kiran Solanki**  
**ARIZONA STATE UNIVERSITY**  
**660 S MILL AVE STE 312**  
**TEMPE, AZ 85281**

---

**08/31/2016**  
**Final Report**

<p><b>DISTRIBUTION A: Distribution approved for public release.</b></p>
---

Air Force Research Laboratory  
AF Office Of Scientific Research (AFOSR)/RTA1

<b>REPORT DOCUMENTATION PAGE</b>					Form Approved OMB No. 0704-0188	
<p>The public reporting burden for this collection of information is estimated to average 1 hour per response, including the time for reviewing instructions, searching existing data sources, gathering and maintaining the data needed, and completing and reviewing the collection of information. Send comments regarding this burden estimate or any other aspect of this collection of information, including suggestions for reducing the burden, to the Department of Defense, Executive Service Directorate (0704-0188). Respondents should be aware that notwithstanding any other provision of law, no person shall be subject to any penalty for failing to comply with a collection of information if it does not display a currently valid OMB control number.</p> <p><b>PLEASE DO NOT RETURN YOUR FORM TO THE ABOVE ORGANIZATION.</b></p>						
1. REPORT DATE (DD-MM-YYYY) 07/22/2016		2. REPORT TYPE Final			3. DATES COVERED (From - To) 03/15/2013 - 03/14/2016	
<b>4. TITLE AND SUBTITLE</b> Hierarchically-Driven Approach for Quantifying Fatigue Crack Initiation and Short Crack Growth Behavior in Aerospace Materials					5a. CONTRACT NUMBER FA9550-13-1-0144	
					5b. GRANT NUMBER	
					5c. PROGRAM ELEMENT NUMBER	
<b>6. AUTHOR(S)</b> K.N. Solanki					5d. PROJECT NUMBER	
					5e. TASK NUMBER	
					5f. WORK UNIT NUMBER	
<b>7. PERFORMING ORGANIZATION NAME(S) AND ADDRESS(ES)</b> ARIZONA STATE UNIVERSITY OFFICE FOR RESEARCH AND SPONSORED PROJECTS 660 S MILL AVE STE 312 TEMPE AZ 85281-3670ADMINISTRATI					<b>8. PERFORMING ORGANIZATION REPORT NUMBER</b>	
<b>9. SPONSORING/MONITORING AGENCY NAME(S) AND ADDRESS(ES)</b> USAF, AFRL DUNS 143574726 AF OFFICE OF SCIENTIFIC RESEARCH 875 NORTH RANDOLPH STREET, RM 3112 ARLINGTON VA 22203 SHANE C. LOMELIN (703) 588-0196					<b>10. SPONSOR/MONITOR'S ACRONYM(S)</b>  AFOSR	
					<b>11. SPONSOR/MONITOR'S REPORT NUMBER(S)</b>	
<b>12. DISTRIBUTION/AVAILABILITY STATEMENT</b> DISTRIBUTION A: Distribution approved for public release.						
<b>13. SUPPLEMENTARY NOTES</b>						
<b>14. ABSTRACT</b>						
<b>15. SUBJECT TERMS</b>						
<b>16. SECURITY CLASSIFICATION OF:</b>			<b>17. LIMITATION OF ABSTRACT</b>  UU	<b>18. NUMBER OF PAGES</b>  36	<b>19a. NAME OF RESPONSIBLE PERSON</b> Kiran Solanki	
a. REPORT U	b. ABSTRACT U	c. THIS PAGE U			<b>19b. TELEPHONE NUMBER (Include area code)</b> 480-965-1869	

## INSTRUCTIONS FOR COMPLETING SF 298

**1. REPORT DATE.** Full publication date, including day, month, if available. Must cite at least the year and be Year 2000 compliant, e.g. 30-06-1998; xx-06-1998; xx-xx-1998.

**2. REPORT TYPE.** State the type of report, such as final, technical, interim, memorandum, master's thesis, progress, quarterly, research, special, group study, etc.

**3. DATES COVERED.** Indicate the time during which the work was performed and the report was written, e.g., Jun 1997 - Jun 1998; 1-10 Jun 1996; May - Nov 1998; Nov 1998.

**4. TITLE.** Enter title and subtitle with volume number and part number, if applicable. On classified documents, enter the title classification in parentheses.

**5a. CONTRACT NUMBER.** Enter all contract numbers as they appear in the report, e.g. F33615-86-C-5169.

**5b. GRANT NUMBER.** Enter all grant numbers as they appear in the report, e.g. AFOSR-82-1234.

**5c. PROGRAM ELEMENT NUMBER.** Enter all program element numbers as they appear in the report, e.g. 61101A.

**5d. PROJECT NUMBER.** Enter all project numbers as they appear in the report, e.g. 1F665702D1257; ILIR.

**5e. TASK NUMBER.** Enter all task numbers as they appear in the report, e.g. 05; RF0330201; T4112.

**5f. WORK UNIT NUMBER.** Enter all work unit numbers as they appear in the report, e.g. 001; AFAPL30480105.

**6. AUTHOR(S).** Enter name(s) of person(s) responsible for writing the report, performing the research, or credited with the content of the report. The form of entry is the last name, first name, middle initial, and additional qualifiers separated by commas, e.g. Smith, Richard, J, Jr.

**7. PERFORMING ORGANIZATION NAME(S) AND ADDRESS(ES).** Self-explanatory.

**8. PERFORMING ORGANIZATION REPORT NUMBER.**

Enter all unique alphanumeric report numbers assigned by the performing organization, e.g. BRL-1234; AFWL-TR-85-4017-Vol-21-PT-2.

**9. SPONSORING/MONITORING AGENCY NAME(S) AND ADDRESS(ES).** Enter the name and address of the organization(s) financially responsible for and monitoring the work.

**10. SPONSOR/MONITOR'S ACRONYM(S).** Enter, if available, e.g. BRL, ARDEC, NADC.

**11. SPONSOR/MONITOR'S REPORT NUMBER(S).** Enter report number as assigned by the sponsoring/monitoring agency, if available, e.g. BRL-TR-829; -215.

**12. DISTRIBUTION/AVAILABILITY STATEMENT.** Use agency-mandated availability statements to indicate the public availability or distribution limitations of the report. If additional limitations/ restrictions or special markings are indicated, follow agency authorization procedures, e.g. RD/FRD, PROPIN, ITAR, etc. Include copyright information.

**13. SUPPLEMENTARY NOTES.** Enter information not included elsewhere such as: prepared in cooperation with; translation of; report supersedes; old edition number, etc.

**14. ABSTRACT.** A brief (approximately 200 words) factual summary of the most significant information.

**15. SUBJECT TERMS.** Key words or phrases identifying major concepts in the report.

**16. SECURITY CLASSIFICATION.** Enter security classification in accordance with security classification regulations, e.g. U, C, S, etc. If this form contains classified information, stamp classification level on the top and bottom of this page.

**17. LIMITATION OF ABSTRACT.** This block must be completed to assign a distribution limitation to the abstract. Enter UU (Unclassified Unlimited) or SAR (Same as Report). An entry in this block is necessary if the abstract is to be limited.

## Contract Information

Contract Number	FA9550-13-1-0144
Title of Research	Hierarchically-Driven Approach for Quantifying Fatigue Crack Initiation and Short Crack Growth Behavior in Aerospace Materials
Principal Investigator	K.N. Solanki
Organization	Arizona State University
Project Start Date	March 15 <sup>th</sup> 2013

## Technical Section

### *1. Technical Objectives*

The objective of this three-year research project is to qualitatively and quantitatively map the relationship between GB characters (structure) and material cohesive strengths with fatigue crack initiation and SCG mechanisms (initiation and growth versus resistance).

### *2. Final summary*

Here, we present a hierarchical form of multiscale modeling to understand fundamental issues of deformation in Ti. This report presents our effort in the following areas,

1. Effects of oxygen on prismatic faults in  $\alpha$ -Ti: A combined quantum mechanics/molecular mechanics study
2. Nano-indentation and slip transfer (critical in understanding crack initiation)
3. An extended-finite element framework (XFEM) to study SCG mechanisms
4. Atomistic methods to develop a grain and twin boundaries database in  $\alpha$ -Ti to quantify and develop
  - a. a crack initiation model,
  - b. the necessary cohesive zone models for interfaces and single crystals, and
  - c. a crystal plasticity model

Fundamental to the development of a hierarchical atomistic-continuum methodology for SCG is the development of appropriate crack initiation models, cohesive zone properties, crystal plasticity models, and the microstructure based finite element framework, i.e., in this case, we are using an XFEM. Overall, we have generalized XFEM to include implicit representation of grains and grain boundaries. The new formulation can incorporate microstructure features directly based on EBSD data using level set formulations. Furthermore, an atomistic database of interactions of dislocation-impurities was developed. Using the developed database an appropriate crystal plasticity model was developed to investigate SCG in Ti alloys.

### **3. Technical details**

#### **3.1 Effects of oxygen on prismatic faults in $\alpha$ -Ti: A combined quantum mechanics/molecular mechanics study**

Titanium (Ti) and its alloys have been traditionally used for structural applications in automotive, aerospace, and biomedical applications due to their high strength-to-weight ratios [1]. Commercially pure Ti-alloys are particularly attractive due to their excellent corrosion resistance, light weight, and formability. Crucial to the mechanical properties of these alloys is the presence of oxygen impurities. Specifically, it has been shown that the oxygen impurities can either harden or soften the materials as a result of the interaction between the impurities and lattice defects, particularly dislocations and twins [2–4]. In high strength grade Ti-alloys the addition of oxygen improves the corrosion and wear resistance of  $\alpha$ -Ti and its alloys [1,5]. However, at elevated temperatures an oxide layer at the Ti surface is formed and the oxygen atoms can diffuse rapidly into the base metal [4] instigating hardening and embrittlement of the base material [3]. In particular, a dislocation core could act as a fast path for diffusing oxygen atoms whose mobility can be orders of magnitude higher than those in bulk diffusion, and this phenomenon is often referred to as “pipe diffusion”. By creating a short-circuit pathway the pipe diffusion can affect many kinetic processes in the bulk materials, including creep, [6] dynamic-strain aging, crystallization [7], and other mechanical properties of  $\alpha$ -Ti. Consequently, understanding the atomistic mechanisms behind oxygen-metal interaction is crucial for developing high-performance Ti alloys [2,8,9] with applications in nuclear power plants, wind turbines, and other large-scale industrial infrastructure.

In this report we examine oxygen diffusion in bulk  $\alpha$ -Ti and pipe diffusion along a prismatic edge dislocation core. In addition, we evaluate the dislocation mobility in the presence and absence of oxygen impurities. We have employed a coupled quantum mechanics and molecular mechanics (QM/MM) method that combines the accuracy of QM calculations with the simplicity and efficiency of MM simulations. In conjunction with a climb-based nudged elastic band (C-NEB) method [10] we can determine the oxygen diffusion barriers accurately. More specifically, the QM/MM model is partitioned into two spatial domains: a QM region consisting of the dislocation core and the oxygen impurity and an MM region for the rest of the system. In the QM region the energy and force are calculated based on the density functional theory (DFT) [11,12] as implemented in the Vienna Ab-initio Simulation Package (VASP) [13] while the same quantities

in the MM region are computed by empirical atomistic simulations [14] based on the embedded atom method (EAM) due to Zope and Mishin [15]. The coupling between the QM and MM regions is accomplished by the constrained DFT [16]. The post processing of the simulation data is performed using OVITO [17]. Complementary to the atomistic simulations, the Semi-discrete Variational Peierls-Nabarro model (SVPN) [18] was also used to analyze the dislocation core structure and mobility. The chemical interaction between the O impurity and the dislocation core is captured by the so-called generalized stacking fault energy (GSFE) surface which was determined from DFT-VASP calculations. By taking the chemical interaction into consideration the SVPN model can predict the dislocation core structure and mobility in the presence and absence of the O impurity and thus reveal the effect of O on the softening/hardening behavior in  $\alpha$ -Ti.

An edge dislocation was created, as described by Osetsky and Bacon [19], initially in LAMMPS [20]. The edge dislocation structure obtained using the EAM potential was further relaxed using the QM/MM method with 30 meV/Å and 1 meV as the force and energy convergence criterion respectively. The QM region had 196 atoms containing the dislocation core with/without an oxygen impurity and the MM region consisted of 11,926 atoms capturing the long-range elastic field of the dislocation. The overall dimensions of different regions were: 30 Å x 27 Å x 9.26 Å for the QM region and 143.67 Å x 155.07 Å x 9.26 Å for the MM region. The simulations were performed on a rectangular cell having  $x$ ,  $y$ , and  $z$ -axes oriented along the  $[1\bar{2}10]$ ,  $[10\bar{1}0]$ , and  $[0001]$  directions, respectively. The length along the dislocation line  $[0001]$  was set to  $2c$  ( $c = 4.645$  Å) to avoid the interaction of oxygen atoms due to periodic boundary conditions.

For the DFT part, projector augmented wave (PAW) [21] potentials were used to represent the nuclei core with valence electrons on  $s$  and  $d$  orbitals for  $\alpha$ -Ti and valence electrons on  $s$  and  $p$  orbitals for oxygen atoms. Exchange and correlation was treated with GGA using the PBE [22] form with an energy cutoff of 289 eV and the Monkhorst Pack  $k$ -point mesh of  $1 \times 1 \times 5$  along the  $[1\bar{2}10]$ ,  $[10\bar{1}0]$ , and  $[0001]$ , respectively. For GSFE calculations the  $k$ -point mesh was  $18 \times 1 \times 10$  along the  $[1\bar{2}10]$ ,  $[10\bar{1}0]$ , and  $[0001]$ , respectively. A single oxygen atom was introduced on the prismatic shearing plane with 1/6 monolayer (ML) oxygen concentration; the slip direction is along  $[1\bar{2}10]$ . The oxygen atom was free to relax in all directions; whereas, Ti atoms were free to move along the  $[10\bar{1}0]$  direction only.

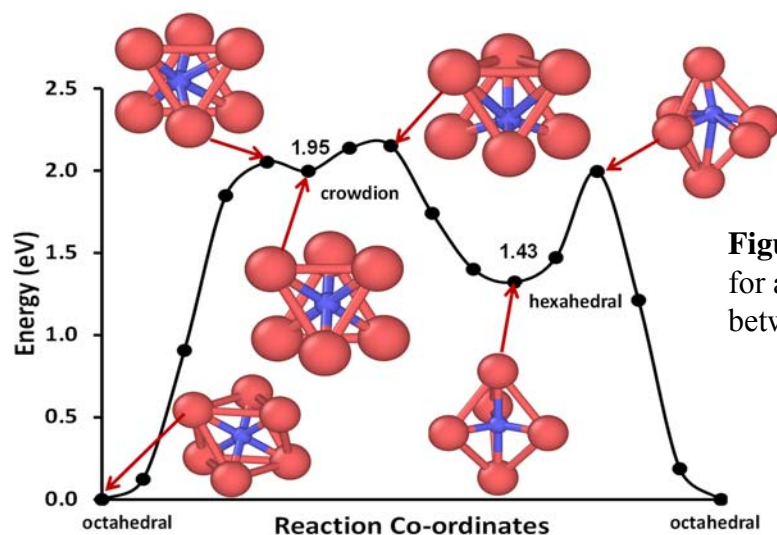
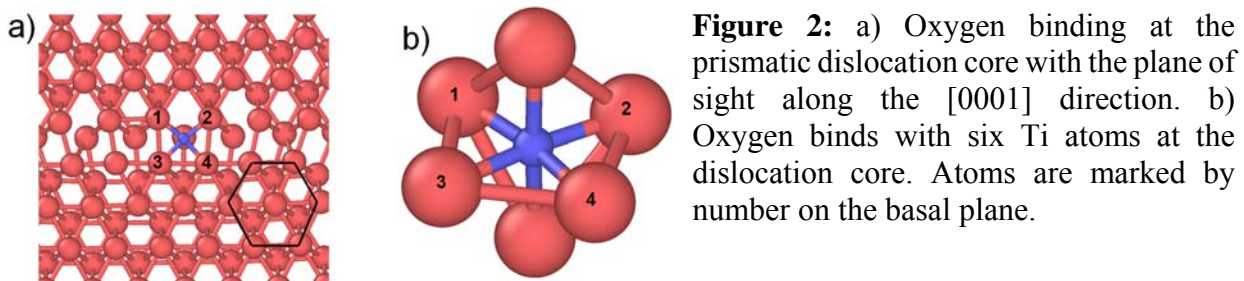


**Figure 1:** C-NEB path and energy barriers for an oxygen atom diffusing in bulk  $\alpha$ -Ti between the interstitial sites.

First we focus on oxygen diffusion in bulk  $\alpha$ -Ti. There are three interstitial positions, octahedral, crowdion, and hexahedral sites, which the O may occupy, and the preferred position is the octahedral site [8]. The hexahedral site is on the basal plane; whereas, the octahedral and crowdion sites are between the A and B stacking along the [0001] direction [8]. The transition pathways and energy barriers between the different interstitial sites for a diffusing O atom have been determined using the C-NEB method with 4 intermediate images. Figure 1 shows the energy barriers for the O atom diffusing from an octahedral site to an adjacent crowdion site (O-C) and subsequently from a crowdion position to a hexahedral position (C-H) and finally from a hexahedral position to an octahedral position (H-O). Also in Figure 1, the diffusion pathway is illustrated by showing the oxygen positions along the transition path. The potential energy of the hexahedral site is 1.43 eV higher than that of the octahedral site. Moreover the excess energy of the crowdion site over the octahedral site is 1.95 eV. Both crowdion and hexahedral sites are local energy minima and thus excess thermal energy is required for the O atom to reach the octahedral sites. The diffusion energy barriers from the crowdion and the hexahedral sites to the octahedral sites are 120 meV and  $\sim$ 550 meV respectively. Both compare well with the work of Wu and Trinkle [8].



Next we study oxygen-dislocation interaction in  $\alpha$ -Ti. To this end we first need to determine the relative site preference of oxygen at the dislocation core. The total energy of a single oxygen atom placed at various interstitial sites near and away from the dislocation core has been calculated. Figure 2a shows the optimized equilibrium geometry of the oxygen at the prismatic edge dislocation in  $\alpha$ -Ti viewed along the  $[0001]$  direction. It is found that the local atomic configuration changes from an HCP octahedral to a BCC octahedral structure. The oxygen atom binds with four Ti atoms on the same basal plane and with two Ti atoms above and below the plane. The O position is the same as in the hexahedral site in bulk  $\alpha$ -Ti except that now there are four atoms on the basal plane (see Figure 2b) instead of three (Figure 1).

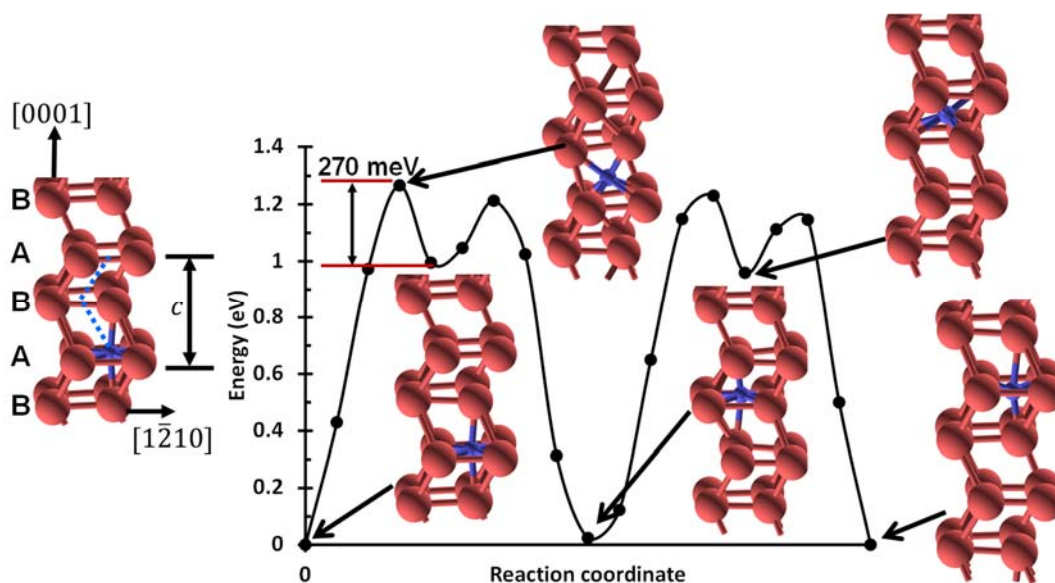


**Figure 3:** a) Diffusion path of an oxygen atom along the dislocation line ( $[0001]$  direction) of the prismatic edge dislocation with ABAB stacking sequence. b) The C-NEB path for an oxygen atom diffusing along the dislocation line.



Having obtained the stable oxygen site at the dislocation core, we proceed to determine the oxygen diffusion pathway and energy barriers along the dislocation core using the C-NEB method with 16 intermediate images. Figure 3a shows the initial path for an oxygen atom to diffuse over a distance of  $c$  (4.645 Å) in the dislocation line direction of  $[0001]$  with ABAB stacking. The energy barrier and diffusion path for the pipe diffusion of oxygen along the dislocation line are depicted in Figure 3b. Also the migration pathway is illustrated by showing the oxygen position along the path in Figure 3b. The energy barrier for the diffusion path from one BCC octahedral position to another BCC octahedral position is 1.24 eV which is much smaller than the bulk diffusion barrier of 2.0 eV. To put the results in perspective we can estimate the required temperature for an oxygen atom jumping from one octahedral site to the next in the bulk  $\alpha$ -Ti and for the pipe diffusion along the dislocation line. Assuming the phonon frequency as  $10^{13} \text{ s}^{-1}$  and for a unit probability, the required temperature for the bulk diffusion is 775 K, much higher than that of the pipe diffusion at 496 K.

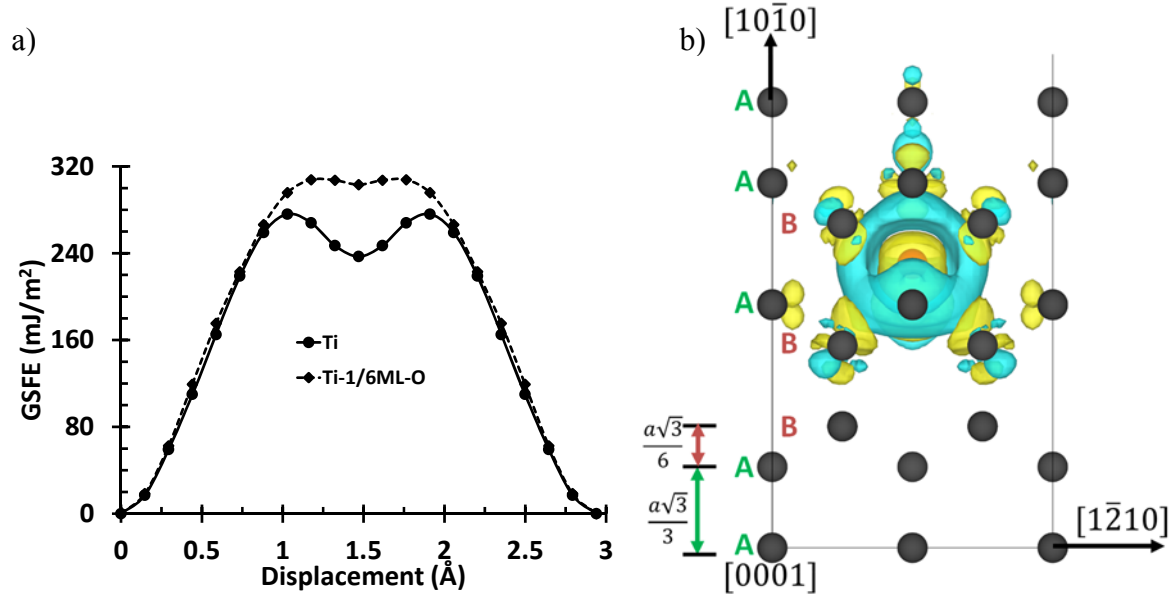


**Figure 4:** a) GSFE as a function of shear displacement along the  $[1\bar{2}10]$  direction of  $\alpha$ -Ti with and without 1/6 ML oxygen on the slip plane. b) A 3D iso-surface plot for charge density showing the effect of O at the prismatic stacking fault. The orange and black atoms represent oxygen and Ti atoms respectively. The yellow and cyan iso-surfaces represent charge accumulation and depletion respectively.

Next we examine the effect of oxygen on the deformation behavior  $\alpha$ -Ti using the SVPN model in conjunction with the *ab initio* determined GSFE. Figure 4a illustrates the GSFE curves as a function of the shear displacement in the  $[\bar{1}210]$  direction with (the oxygen concentration is 1/6 ML) and without the interstitial oxygen. The unstable stacking fault energy is increased from 237 mJ/m<sup>2</sup> to 303 mJ/m<sup>2</sup> (28% increase) in the presence of oxygen on the shear plane. The dislocation core width and the Peierls stress were calculated using the SVPN method with *ab initio* GSFE. The Peierls stress for the prismatic edge dislocation with and without oxygen was found to be 97 MPa and 24 MPa respectively (~400% increase). The simulations also revealed that the prismatic dislocation becomes narrower in the presence of oxygen, from 1.1 Å to 0.9 Å. This narrowing of the core width is consistent with the increase of the Peierls stress since the Peierls stress depends exponentially on the ratio between the dislocation core width and the atomic spacing along the dislocation line.

The mechanical properties of a material are determined by the nature of atomic bonding; therein, both the shear strength and cohesive energy are affected by the directionality and strength of chemical bonds. Therefore, understanding the change in charge density resulting from a solute atom can shed light on the strengthening mechanism of the impurity (see [23]). Figure 4b presents a 3D iso-surface plot for the differential charge density in the presence of the oxygen atom. The yellow and cyan iso-surfaces represent charge accumulation and depletion respectively. Compared to the charge density distribution in pure  $\alpha$ -Ti the main change due to oxygen happens around the octahedral site as seen in Figure 4b. The charge densities between Ti atoms were evidently increased with the addition of oxygen resulting in an increase in the shear modulus which affects the dislocation mobility.

In summary, the oxygen-metal interaction in  $\alpha$ -Ti was examined including oxygen diffusion barriers and oxygen effects on the prismatic edge dislocation ( $\{10\bar{1}0\}\langle\bar{1}210\rangle$ ) motion. It was found that oxygen prefers to occupy the BCC octahedral site at the dislocation core. Moreover, the oxygen diffusion barrier along the edge dislocation line from a BCC octahedral position to an HCP octahedral position is 1.24 eV which is much smaller than the bulk diffusion barrier of 2.0 eV. We show that a one-sixth monolayer of oxygen addition increases the Peierls stress by four-times and reduces the dislocation core width by 18%. The charge densities between Ti atoms were increased

with the addition of oxygen at the prismatic fault resulting in an increase in the shear modulus. The calculated hardening effect of oxygen and oxygen diffusion barriers are consistent with those experimentally observed [3]. Overall our study provides critical knowledge towards a comprehensive understanding of oxygen effects on the deformation behaviors of  $\alpha$ -Ti.

### 3.2 Grain boundary energy and structure in $\alpha$ -Ti

Grain boundaries are two-dimensional defects which are characterized by five macroscopic degrees of freedom [24–31]. Saylor *et al.* [24] analyzed the GB character distribution (GBCD) in commercially pure Al and suggested that boundaries with low index planes occur with particularly high frequency in polycrystals. The GB structure-energy correlation in several FCC metals was investigated by Wolf [32] who established a linear relationship between GB energy and volume expansion per unit area (grain boundary free volume). The role of the GB plane in determining GB energy was investigated by Holm *et al.* [26], who performed extensive calculations of GB energies in Ni and Al. Rohrer [33] established that the coincidence lattice site density ( $\Sigma$ ) plays only a minor role as a determinant of GB energy in several systems and that the energies of the crystal surfaces that meet at a GB is a better indication of GB energy. Solanki *et al.* found that certain defects are favored at  $\alpha$ -Fe grain boundaries and that these species affect the grain boundary cohesive strength [34]. Experimentally, grain boundary structure has been observed using field ion microscopy and high resolution transmission electron microscopy [35–40]. The grain boundary energies can be computed through theoretical formulations and computational methods. Thus, understanding the atomic structure at the grain boundary can provide insight into the grain boundary strength as well as various grain boundary dependent phenomena, such as dislocation pileup and crack initiation site [41].

Understanding the structure and energy of the grain boundary system is crucial for engineering materials intended for advanced applications because grain boundary properties can vary widely (coherent twin versus low-angle versus high-angle grain boundaries). Grain boundaries with certain misorientation angles (and typically a low  $\Sigma$  value) correspond to “favored” structural units, while other boundaries are characterized by structural units from the two neighboring favored boundaries. Also, different grain boundaries can be characterized according to their energy and can be correlated to the behavior at the atomic level. In the first year of this project, a range of grain boundary structures and energies that are representative of some of the variation observed in

the grain boundary character distribution of polycrystalline Ti was generated to be used in investigating the role of grain boundary character on

1. slip transfer behavior (crack initiation)
2. cohesive zone properties (crack growth)
3. non-Schmid behavior (dislocation versus twin, crystal plasticity formulation)

Initially, a database of 61 minimum energy symmetric tilt grain boundaries (STGBs) of Ti, with the tilt axes as  $[1\bar{2}10]$  and  $[0\bar{1}10]$  was generated with molecular static simulations, which were performed using the classical molecular dynamics code Large-scale Atomic/Molecular Massively Parallel Simulator (LAMMPS) [42]. Here, the analysis cell consisted of a standard bicrystal cell with a single grain boundary that divides the HCP crystal into two single crystals, as shown in Figure 1a. The initial single crystals were created with  $x$ ,  $y$  and  $z$  along the  $[0\bar{1}10]$ ,  $[0001]$ , and  $[1\bar{2}10]$  directions, respectively, for the  $[1\bar{2}10]$  tilt axis; and along the  $[1\bar{2}10]$ ,  $[0001]$ , and  $[0\bar{1}10]$  directions, respectively, for the  $[0\bar{1}10]$  tilt axis. Then, the upper half crystal was rotated clockwise and the lower half crystal counter-clockwise by angle  $\theta$  with respect to the tilt axis, as shown in Figure 5b. Several successive rigid body translations, followed by an atom-deletion technique and energy minimization using a non-linear conjugate method [43–45] were used to generate the final relaxed minimum structure with the grain boundary plane along the  $x$ - $z$  plane, as shown in Figure 5c. This procedure was replicated to generate several 0 K minimum-energy grain boundary structures for Ti. Here, we used the MEAM potential of Hennig et al. [46].

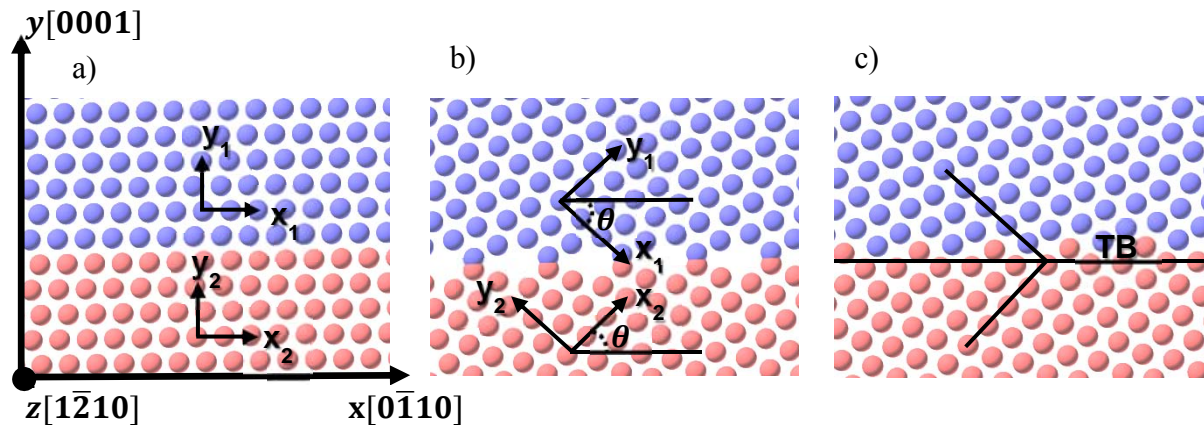


**Figure 5:** (a) Single crystal model with  $x$ ,  $y$  and  $z$  along the  $[0\bar{1}10]$ ,  $[0001]$ , and  $[1\bar{2}10]$  directions, respectively; (b) Upper half of crystal rotated  $\theta$  ( $\sim 42^\circ$ ) clockwise and lower half of crystal rotated

counter-clockwise; and (c) Final grain boundary structure: rotated crystal is minimized with 1 pN force on each atom using a conjugate gradient algorithm. Note: TB notes the twin boundary.

Figure 6 shows both the grain boundary energy as a function of misorientation angle for the  $[1\bar{2}10]$  STGB system and the variation of GB energy as a function of GB geometry in a stereographic triangle representation, which is widely used to represent cubic systems [32]. The trend observed for the grain boundary energy as a function of a misorientation angle is comparable to what has been previously reported for Ti [47]. The stereographic representation of GB energies for the entire misorientation range helps to identify GBs that show a local minima in GB energies in the energy-misorientation plot (refer to Figure 6b).

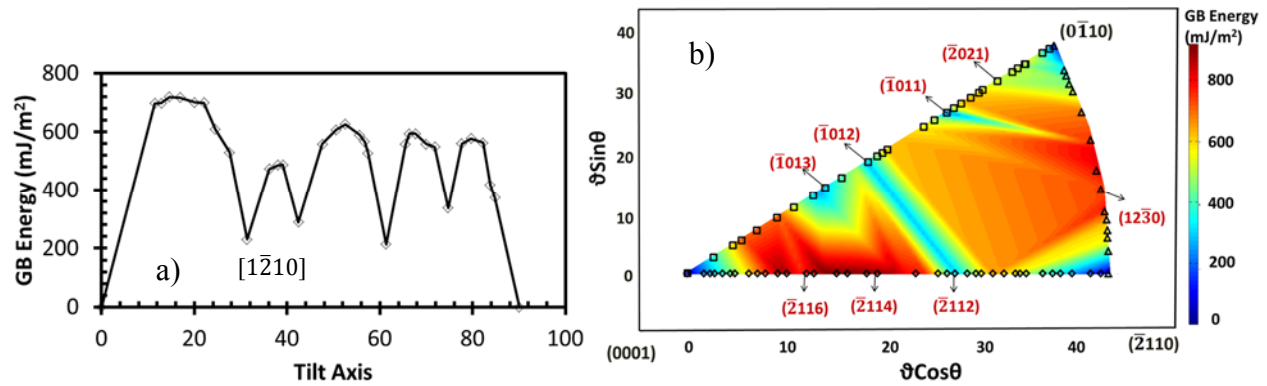


**Figure 6:** (a) Grain boundary energy for the  $[1\bar{2}10]$  symmetric tilt grain boundary system. (b) Contour plot of GB energies for the three symmetric tilt systems of Ti represented using polar and azimuthal angles. The polar and azimuthal angles correspond to the degrees of freedom.

The structure-energy correlation can provide more details about the variation in grain boundary energies, as each grain boundary has characteristic structural units (SUs) describing its atomistic morphology. Low-angle boundaries can be represented by an array of discrete dislocations. However, at higher misorientation angles (high-angle grain boundaries), the dislocation cores overlap, and dislocations rearrange to minimize the boundary energy. The resulting grain boundary structures are often characterized by grain boundary dislocations or SUs [47–49]. Figure 7 shows the spatial distribution of atomic excess volume for  $(\bar{1}011)[1\bar{2}10]$ ,  $(\bar{2}021)[1\bar{2}10]$ ,  $(\bar{2}112)[0\bar{1}10]$ , and  $(\bar{2}116)[0\bar{1}10]$  grain boundaries. Notice that the atoms far away from the boundary are green, indicating that there is no atomic volume difference over the bulk lattice. The

bulk Voronoi volume was found to be  $17.57 \text{ \AA}^3$  for the Ti. The excess Voronoi volume is highest/lowest (tensile versus compressive) at the grain boundary center and converges to the bulk Voronoi volume as distance from the grain boundary increases. This grain-boundary metric can in turn be correlated to other energetics associated with the grain boundaries to derive a structure-property relationship. The developed grain boundary database will be applied to investigating the role of grain boundary character on (a) slip transfer behavior (crack initiation); (b) cohesive zone properties (crack growth); and (c) non-Schmid behavior (dislocation versus twin, crystal plasticity formulation)

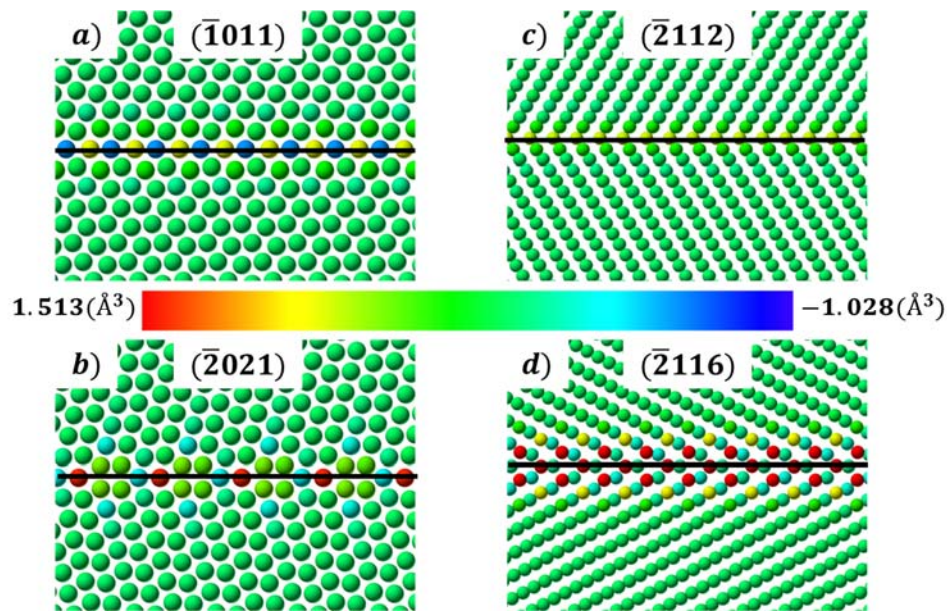


**Figure 7:** Atomic representation of (a)  $(\bar{1}011)[1\bar{2}10]$ , (b)  $(\bar{2}021)[1\bar{2}10]$ , (c)  $(\bar{2}112)[0\bar{1}10]$  and (d)  $(\bar{2}116)[0\bar{1}10]$  grain boundaries depicting the distribution of the excess Voronoi volume. The bulk Voronoi volume was found to be  $17.57$ . The black line indicates the twin boundary plane.

### 3.3 Atomistic study of the dislocation-grain boundary interaction

The short fatigue crack propagation behavior is significantly altered in the presence of microstructural features. Grain boundaries play a fundamental role in determining the strengthening mechanisms as they act as an impediment to dislocation motion [50,51]. The presence of grain boundary that presents a large barrier to plastic flow leads to generation of dislocation pileups. A simple geometry of a grain with the basal plane inclined to the applied axis



and a TB-dislocation interaction model are shown in Figures 8a and 8b, respectively. There are four possible outcomes of slip-grain boundary interactions (Figure 9) i.e. a) a direct transmission; b) a direct transmission with a residual dislocation along the grain boundary; c) an indirect transmission with a residual dislocation occurring because the incoming and outgoing slip planes do not intersect; and d) no transmission because the dislocation is absorbed at the grain boundary. Furthermore, the slip-grain boundary interactions can be summarized in terms of the Burgers vector of the incident ( $b_i$ ), transmitted ( $b_t$ ) and the residual dislocations ( $b_r$ ).

$$\vec{b}_i \rightarrow \vec{b}_t + \vec{b}_r$$

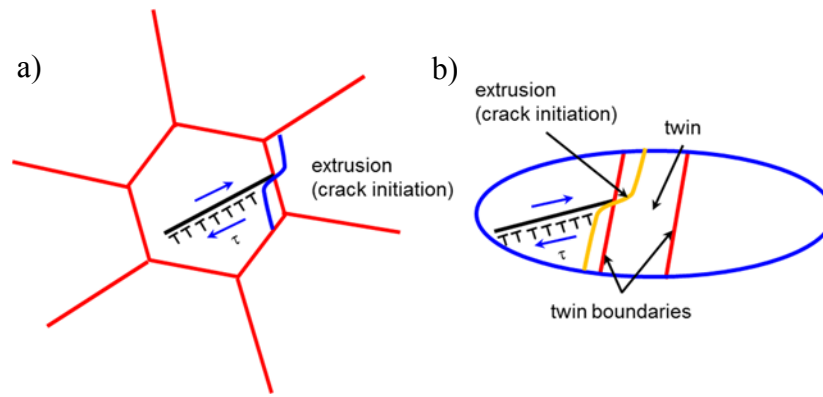


**Figure 8:** (a) A schematic illustrating dislocation pile-up, interaction and extraction at the GBs that leads to static extrusions across the boundary in the form of ledges and steps, and (b) a schematic illustration of a twin lamella with the dislocation interaction that leads to static extrusions across the boundary in the form of ledges and steps.

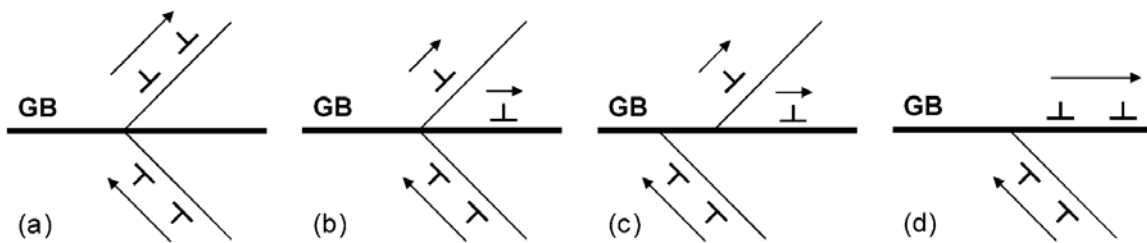


**Figure 9:** Slip-grain boundary interaction cases: (a) a direct transmission and dislocation cross-slip; (b) a direct transmission with a residual dislocation along the grain boundary; (c) an indirect transmission with a residual dislocation, where slip planes in each grain do not intersect; and (d) no transmission.

Several criteria [52–56] have been developed to predict the outcome for the DGB interaction. Shen et al. [54–56] devised a set of rules to predict the slip transmission when: a) the angle of intersection between both the incoming and outgoing slip plane is minimized and b) the resolved shear stress acting along the slip direction is maximized. Further, based on in-situ TEM experiments, Lee et al. [53] proposed an additional criterion to the model of Shen et al. [54–56] that ensures the outcome of slip transmission is based on the minimum residual dislocation along the GB, also known as the Lee-Robertson-Birnbaum (LRB) criteria. The geometric condition for the slip transmission can be expressed by the relative orientations of the slip planes and the GB plane normal in the following manner.

$$M = l_{in} \cdot l_{out} \quad (1)$$

where,  $l$  is the unit normal at the intersection of the incoming and outgoing slip planes with the GB plane.

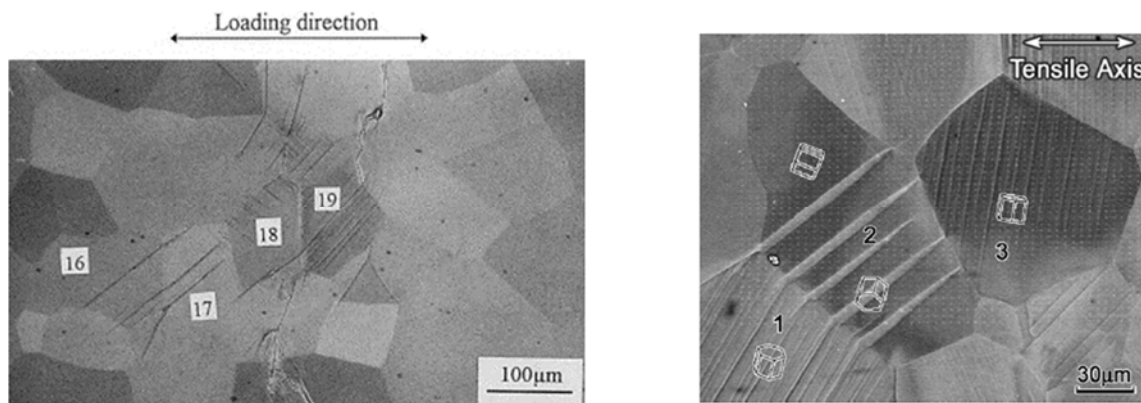


Figure 10: a) slip band cracks across the grain boundary in the case of grain 16 and grain 17 and b) deformation twins in grain 2 appear to have been nucleated at the grain boundary with grain 1. The slip bands in grain 1 and the deformation twins in grain 2 are correlated. This was adopted from Wang et al. [57].

Experimental verifications of these models are difficult because of microstructural heterogeneities introduced during processing which, along with dislocation pile-ups, can significantly alter the DGB interaction. Wang et al. [57] showed formation of cracks due to the interaction of twin-twin and slip band formation as seen in Figure 10a. Moreover, he also has shown deformation twins nucleation from the grain 1-grain 2 grain boundary (Figure 10b) and propagates towards the grain



boundary of grain 2-grain 3 (Figure 10b), based on the difference in the thickness of the twin at the grain boundary of grain 1-grain 2 as compared with the grain boundary of grain 2-grain 3. Furthermore, a slip-twin correlation with the help of the Luster-Morris parameter [58]; wherein, the prismatic slip interacts with the grain boundary and nucleates a deformation twin in the adjacent grain even though the c-axis of the grain is oriented at 45° to the loading axis which is unfavorable for twinning according to the Schmidt factor. Our main objective was to quantify all of the possible outcomes of slip/ twin interaction with the grain boundary interaction.

Further, the atomic level details related to the interaction of individual grain boundaries with dislocations still remain unclear due to insufficient resolution. For example, the GB atomic structures vary spatially which could change the pinning strength of impeding dislocations. This has motivated several atomistic studies in BCC [59,60], FCC [61,62], and HCP [63,64] metals to validate these analytical models. In particular, previous atomistic [61,65] studies have shown that slip transmission was observed to violate the LRB criteria by transmitting on slip planes that did not have the highest resolved shear stress. Based on these findings, it was suggested that the underlying atomic structure at the DGB interaction site plays a key role in determining the outcome [61,62,65]. Despite the large body of work on DGB interactions, there is still a lack of systematic study on the role of grain boundary structure especially in  $\alpha$ -Ti.

Here, we carried out atomistic simulations to examine the DGB interactions across several grain boundaries in  $\alpha$ -Ti using interatomic potential. The energy barrier for slip transmission across the GB was used to quantified by defining a control volume at the site of the DGB interaction [62]. The defected atoms (centrosymmetry parameter [66] > 0.5) within the control volume were used to estimate the energy barrier for slip transmission. The evolution of the net change in energy of the defected atoms during the loading process was quantified by comparing instantaneous energy ( $E_t^i$ ) with reference/initial atomic energy ( $E_r$ ). The net energy was normalized with the atomic volume occupied by defect atoms in the reference configuration:

$$E_{barrier} = \frac{\sum_i^n E_t^i - E_r}{V} \quad (2)$$

where  $V$  represents the total volume of the defected atoms within the control volume in the reference configuration.

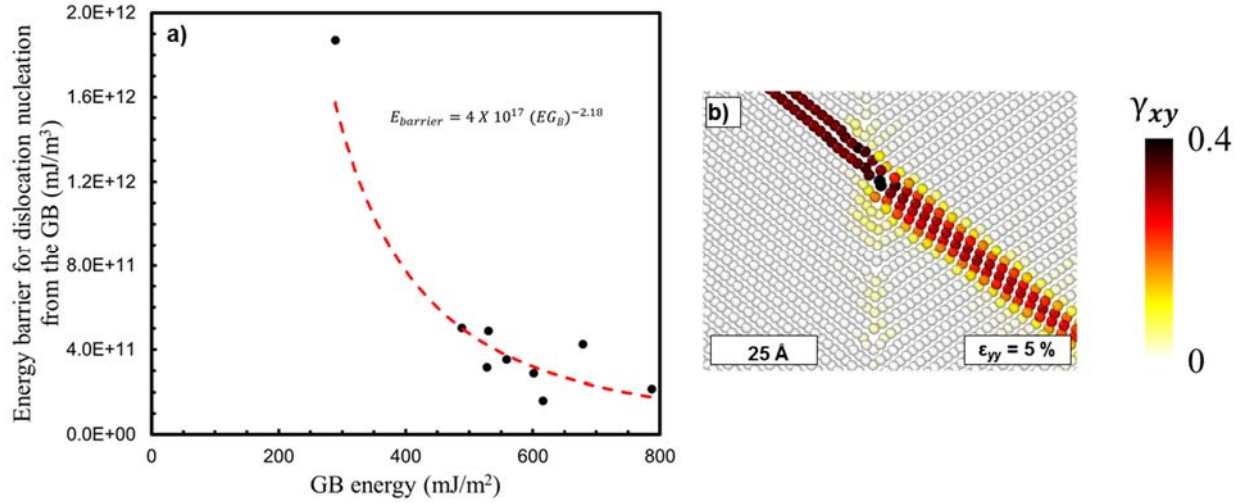


**Figure 11:** a) The dislocation transmission energy barrier across a grain boundary as a function of the grain boundary energy in Titanium. b) The atoms were colored according to the local atomic shear strain ( $\gamma_{xy}$ ) on a scale of 0 to 0.4 showing trace of dislocation glide and nucleation of a twin.

In this work, seven different grain boundaries from the  $[\bar{2}110]$  and  $[0\bar{1}10]$  tilt axes were deformed to study the DGB interaction. A strong inverse relationship between the energy barrier for slip transmission ( $E_{barrier}$ ) and the initial GB energy ( $E_{GB}$ ) was found Figure 11. In other words, GBs with lower interfacial energy demonstrated a higher barrier for slip transmission, which is in agreement with previous study [62]. Figure 11b shows the interaction of the Basal dislocation in grain 1 (soft grain) with the grain boundary. Subsequently, twin nucleates from the DGB interaction site and propagates in neighboring grain (grain 2).

The energy barrier calculations for the dislocation nucleation from various GBs and subsequent slip transfer can be cast into a crack initiation criterion ( $CI$ ), which is a function of the slip band geometry,  $E_{barrier}$ , and slip increment. The total energy for the slip configuration is given by

$$E = a \sum_i (x_i - x_j) b_i b_j h (\rho - \rho_{int}) E_{barrier}, \quad (1)$$

where  $(x_i - x_j)$  are the dislocation positions,  $b$  is the Burgers vector,  $b_i b_j h$  is the slip band geometry,  $a$  is the model dimension constant, and  $(\rho - \rho_{int})$  is the dislocation density term. The crack initiation is predicted by taking the first derivative of the total energy with respect to the dislocation increment as

$$CI = \frac{dE}{dx} \quad (2)$$

To further understand the slip transfer and deformation behavior of polycrystalline materials, we need to investigate the mechanical behavior of the bulk, i.e., the grain interiors and the defects, which in our case, are the grain boundaries. Nanoindentation offers a great advantage in terms of isolating and probing a small volume to investigate the deformation and slip transfer across the grain boundaries. The load-displacement data from nanoindentation coupled with the orientation information obtained through EBSD can help in characterizing a large set of grain boundaries found experimentally. We pick commercially pure Titanium (CP-Ti) as our primary material system. Then we propose to introduce solutes (alpha stabilizing agents such as O) to CP-Ti through processing techniques since it is known that the deformation is very sensitive to the changes in composition of the alloy.

This experimental study is primarily composed of three levels per composition of the alloy. Firstly, the critical resolved shear stress values for slip on the three main systems, namely, basal, prismatic, and pyramidal are analyzed to understand the plastic deformation of CP-Ti. The critical resolved shear stress can be estimated using the load at the pop-in which is observed during indentation of the grain interior region. The Hertzian theory dictates the elastic response and the elastic-plastic transition identified with a discontinuity in the load-displacement curve. This is known as a “pop-in” event [67]. The pop-ins are characteristic of initiation of plastic flow or, in other words, activation of dislocation sources in the indented volume. Secondly, by probing the regions very close to the grain boundary, an additional pop-in event can be observed that is indicative of the interactions between the grain boundaries and the dislocations source. This secondary pop-in occurs at higher loads and thereby after appreciable plastic deformation and corresponds to the transmission of the piled up dislocations (after the initial pop-in event) across the grain boundaries[68]. Previous studies have identified the emission of dislocations on the other side of the boundary for low angle boundaries. However, for high angle boundaries, the transmission was not observed due to the predominance of GB sliding[69,70]. It has been observed that pop-in occurs for a critical ratio between the plastic zone size beneath the indenter to the distance between the indent and the grain boundary plane for a given misorientation angle [71]. Furthermore, the stress intensity factor for slip transfer was reported to increase with the increase in the misalignment of slip systems ( $m'$  parameter)[72]. It has been pointed out by Britton et al. [72] that it is necessary to identify the detailed stress state of the indenter and correlate the

parameters to the grain boundary character better to completely understand the process of slip transfer during nanoindentation. Lastly, pileup topographies will also be imaged through atomic force microscopy to identify the anisotropy in plastic deformation for the various slip systems. By isolating the bulk contribution from the grain boundary contribution, we can quantitatively determine the role of a grain boundary on the slip transfer process.

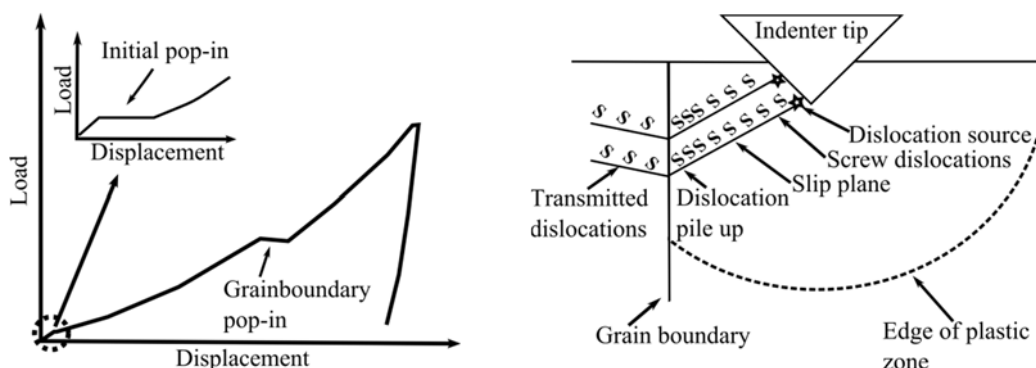


**Figure 12:** Schematic illustration of (a) load-displacement curve with initial and grain boundary pop-in, and (b) direct transmission of dislocations occurring across a grain boundary (adapted from [72])

CP-Ti samples for characterization and testing were machined through electrical discharge machining, and then mechanically ground, polished, and finished with electrochemical polishing. As far as the composition is concerned, the oxygen content was quoted as 0.2 wt.% by the manufacturer. The samples were carefully stored to minimize the effect of ambient air on the surface. As the next step, we characterized the local microstructure of the sample through high resolution EBSD analysis for an area spanning  $600\ \mu\text{m} \times 400\ \mu\text{m}$  (Figure 13). The data was cleaned to reduce erroneous points. Subsequently, regions of interest were identified for nanoindentation. Hysitron Triboscope were used to perform indents on the sample using sphero-conical and berkovich tips. To ensure the accuracy of the test, a sufficient number of indents were made in the grain interior. Care was taken to reduce the effect of grain boundaries and other grains for step 1 that is, computing the critical resolved shear stress of the grain interior (bulk). The other geometrical factors were calculated using the orientation information obtained from EBSD analysis. An illustration indicating the grain boundary and grain indentation scheme is represented in Figure 13. Topography around the indents were measured using AFM's tapping mode on a scanning probe microscope.

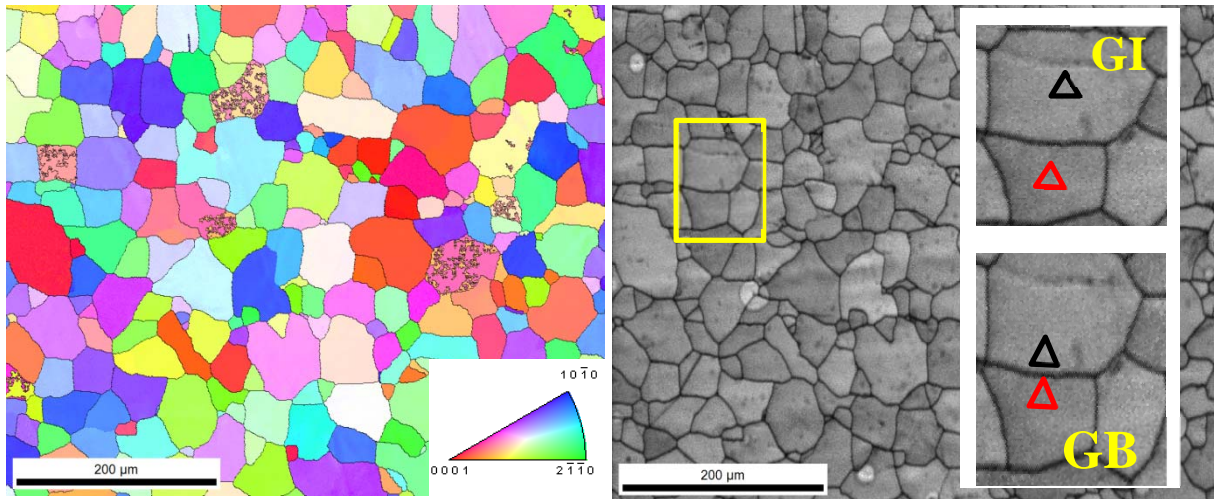


**Figure 13:** (a) High resolution EBSD map of a region from a CP-Ti sample, and (b) representation of grain interior (GI) and grain boundary (GB) indentation scheme

Figure 14 shows the load versus displacement curves of two of the indents made at the grain interior and near the grain boundary for CP-Ti. The indent of the GB was made 2  $\mu\text{m}$  away from the grain boundary. Displacement jumps/strain bursts are evident from the curves at various loads. The first jump occurs at about mN, and it is observed for all the indents made within the grain and close to the grain boundary. The pop-in is characteristic of the transition from the elastic to the plastic regime which can be associated with the stress required for dislocation nucleation. Multiple indentations on several grains were used to estimate the critical resolved shear stress for various slip systems. The average CRSS values for three slip systems (prismatic: basal: pyramidal  $\langle c+a \rangle$ ) was computed to be 181:209:474 MPa which is approximately 1:1.26:2.45. This is consistent with the values reported in the literature (1:1.2:2.62) where prismatic was found to be easily activated for slip in CP-Ti material system. In case of indents close to the grain boundary, there occurs a second pop-in similar to Figure 14 (b) at higher loads (in this case) which is dependent on the distance of the grain boundary to the indent and orientation of the GB. The radius of the elasto-plastic boundary was estimated using the equation proposed by Kramer which takes into account the Pop-in load, and the yield strength of the material. Several values of  $c/d$  were estimated from the indentation data which suggests a critical value of 0.2 to yield pop-ins (based on Johnson's cavity model). The critical stress intensity factor for slip transfer was computed based

on the formulation of Wang et al. suggests a range of values to facilitate slip transfer between grains of varying orientation ( $0.003$  and  $0.41 \text{ MPam}^{0.5}$ ). Although a range of values are reported, these correspond to the different GBs in the material system. The slip systems which are highly aligned facilitate slip transfer and exhibit pop-in behavior have a  $M > 0.98$ .

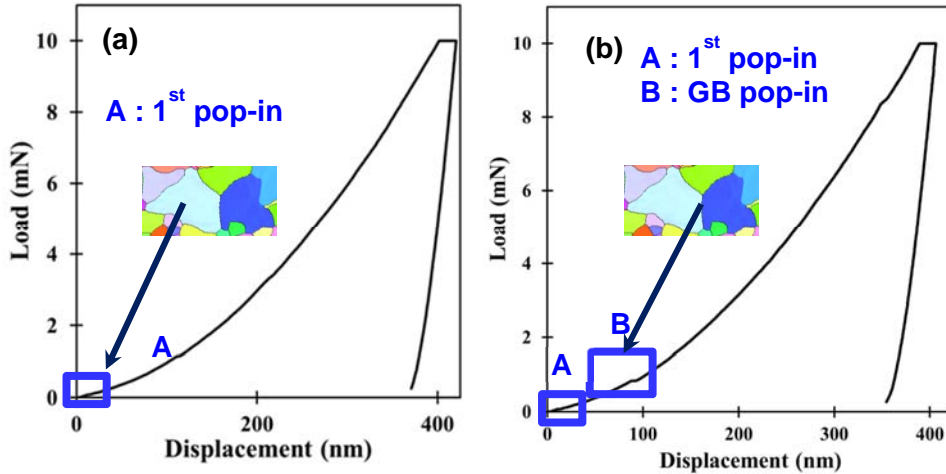


**Figure 14:** Load-displacement curves highlighting the pop-ins in (a) grain interior (GI) and (b) near a grain boundary (GB) in CP-Ti Grade 2 material.

In case of Ti-O sample, several levels of O was introduced through boost diffusion procedure where a CP-Ti sample was subjected to heat treatment under vacuum conditions. Prior to indentation, an EBSD analysis was made to identify the texture and nature of microstructure of the sample (Figure 15). Multiple indentations on the grain interior and near the boundary were made and the first pop-in loads for indents were observed to increase with the increasing O content (Figure 15 (b)). Further, the hardening effect of the O solute is evident from the load-displacement curves and the absence of twinning indicates the increase in the twin formation energy due to the presence of O. The CRSS values for the slip systems revealed a similar ratio as that of pure Ti sample where pyramidal was found to be less activated than prismatic and basal slip systems (pyramidal < bsasl < prismatic). The critical stress-intensity factor for slip transfer revealed a range of values between  $0.001$  and  $0.1 \text{ MPam}^{0.5}$  for the grain boundaries indicating that it is easier for dislocation motion compared to nucleation in the presence of O consistent with atomistic simulations. In-situ SEM characterization of one of the indents indicated in Figure 15 (c) of Ti-O sample reveals the pile-up of the material around the indent.

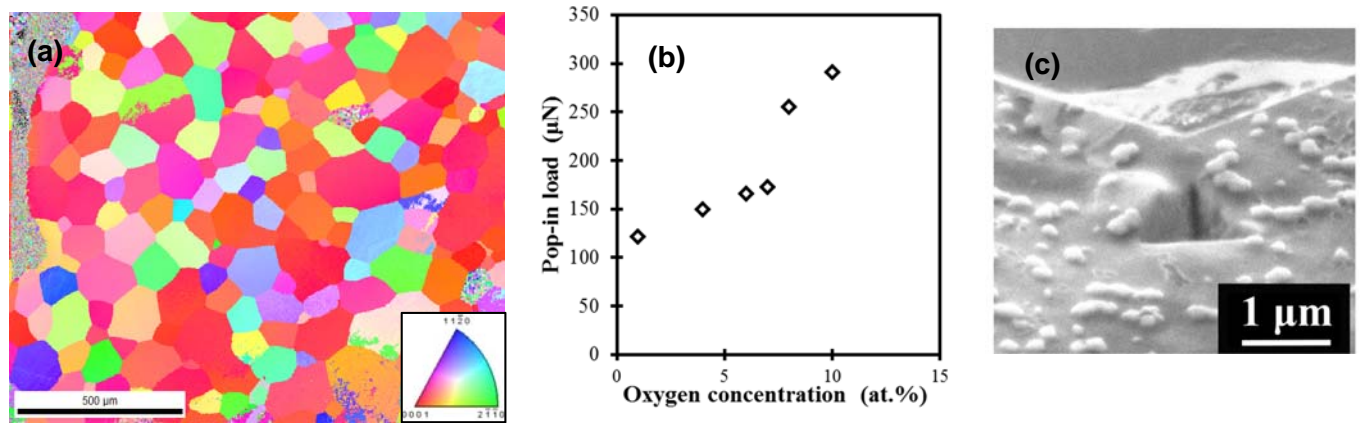


**Figure 15:** (a) High resolution EBSD map of a region from a Ti-O sample, (b) variation in pop-in loads in Ti-O with respect to O concentration, and (c) pile up of material around the indent for in-situ indentation of a grain interior.

### 3.4 Extended finite element framework for the small crack growth

The material fatigue strength of engineering alloys is significantly affected by microstructural variation. For example, fatigue crack initiation and early growth are primary contributing factors to the alloy's total lifespan, and these mechanisms strongly depend on grain boundaries and other defects. Furthermore, microstructural variations such as relative grain orientations influence the cohesive behavior of the grain boundaries, which leads to the crack nucleation and propagation in an intergranular and/or transgranular (see Figure 16) manner [73–76].

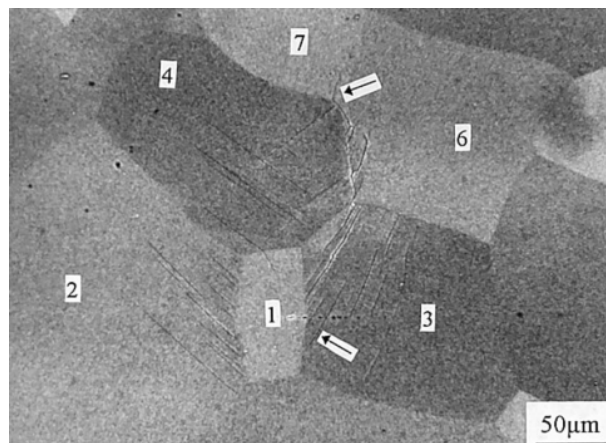


**Figure 16:** Intergranular and transgranular small cracks [73]



The extended finite element method (XFEM) provides a powerful tool for finite element modeling of interfaces **independently** from the computational mesh [77]. To describe the role of microstructure in material failure, some methods have been proposed among which the cohesive finite element method (CFEM) has received much attention [78]. Usually, empirical data for surface decohesion is employed in CFEM to effectively simulate crack initiation or propagation in material. Nevertheless, empirical cohesive laws might be incapable of describing decohesion behavior accurately at sub-micron scales [78]. As an alternative, atomistic simulations can be used to characterize the cohesive behavior of a variety of grain boundaries in order to be used in finite element simulations.

### 3.4.1 XFEM Formulation

As reported before, the suitable XFEM displacement field for modeling a microstructure having strong discontinuities is:

$$\mathbf{u}(\mathbf{x}) = \sum_{I=1}^{N_N} \sum_{i=1}^{N_G} \mathbf{N}_I(\mathbf{x}) H_i(\mathbf{x}) \mathbf{u}_{iI} \quad (1)$$

where in the above equation,  $N_G$  is the number of grains in the microstructure and  $N_N$  is the number of nodes.  $H_i$  is a Heaviside function representing grain  $i$  and is defined as follows:

$$H_i(\mathbf{x}) = \begin{cases} 1 & \mathbf{x} > 0 \\ 0 & \mathbf{x} < 0 \end{cases} \quad (2)$$

For some values of  $I$  and  $i$  and for all values of  $\mathbf{x}$ ,  $\mathbf{N}_I(\mathbf{x})H_i = 0$ . For these combinations,  $\mathbf{u}_{iI}$  is prescribed to be zero and is not stored in the global degrees of freedom. The strong form of equilibrium equations and prescribed boundary conditions are:

$$\nabla \cdot \boldsymbol{\sigma} = 0 \quad \text{on } \Omega \quad (3)$$

$$\boldsymbol{\sigma} = \mathbf{C} : \boldsymbol{\epsilon} \quad (4)$$

$$\boldsymbol{\sigma} \cdot \mathbf{n} = \mathbf{t}_i^0 \quad \text{on } \partial \Omega_{\sigma_i} \quad (5)$$

$$\mathbf{u}_\alpha = \mathbf{u}_i^0 \quad \text{on } \partial \Omega_{u_i} \quad (6)$$

$\mathbf{C}$  and  $\boldsymbol{\epsilon}$  in Eq. 4 are the rank four elasto-plastic stiffness tensor and strain field, respectively. Additionally, at the grain boundaries of each grain ( $\partial \Omega_{gb}$ ), we require that:

$$\boldsymbol{\sigma} \cdot \mathbf{n} = \mathbf{t}_i \quad \text{on } \partial \Omega_{gb_i} \quad (7)$$

for  $i = 1, 2, \dots, N_G$ . We assume a traction-separation constitutive law at the grain boundaries of each grain to have the following form:



$$\mathbf{t}_i = \mathbf{T}_i \cdot \llbracket \mathbf{u}_i \rrbracket \quad (8)$$

where  $\mathbf{T}$  is a second-order constitutive tensor and  $\llbracket \cdot \rrbracket$  denotes the displacement jump at the grain boundary. Displacement jump ( $\llbracket \mathbf{u} \rrbracket$ ) in Eq. 8 for two adjacent grains such as Grain  $a$  and Grain  $b$  at point  $a$  (or point  $b$ ) on the interface (grain boundary  $ab$ ) is defined as follows (see Figure 17):

$$\llbracket \mathbf{u}(\mathbf{x}) \rrbracket_{ab} = \mathbf{u}_a(\mathbf{x}) - \mathbf{u}_b(\mathbf{x}) \quad (3)$$

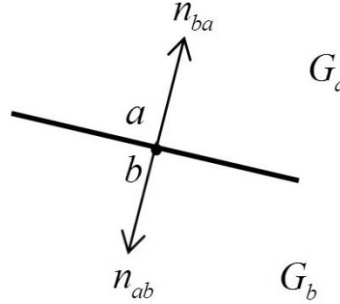


**Figure 17:** Discontinuous grain boundary

The weak form equation is simplified as follows:

$$\int_{\Omega_a} \hat{\epsilon}_a : \mathbf{C} : \epsilon_a \, dv + \sum_b \int_{\partial \Omega_{gb_a}} \mathbf{w}_a \cdot \mathbf{T}_{ab} \cdot (\mathbf{u}_a - \mathbf{u}_b) \, ds = \int_{\partial \Omega_a} \mathbf{w}_a \cdot \mathbf{t}_a^0 \, ds \quad (4)$$

where subscript  $b$  is the number of any grain sharing an interface with grain  $a$  and  $\hat{\epsilon}_a$  is the strain field corresponding to the virtual displacement.

### 3.4.2 Finite element discretization

The discretized form of the equilibrium equation can be derived from the weak form in Eq. 9 and the enriched displacement field of Eq. (1):

$$\mathbf{f}^{\text{int}} = \lambda \mathbf{f}^{\text{ext}} + \mathbf{f}^{\text{coh}} \quad (10)$$

where:

$$\mathbf{f}^{\text{int}} = \int_{\Omega_a} H_a \mathbf{B}^T \{ \mathbf{C} \} \mathbf{B} H_a \, dv \cdot \mathbf{u}_a \quad (11)$$

$$\mathbf{f}^{\text{coh}} = \sum_b \int_{\partial \Omega_{gb_a}} H_a \mathbf{N}^T \cdot \mathbf{T}_{ab} \cdot (\mathbf{N} H_a \mathbf{u}_a - \mathbf{N} H_b \mathbf{u}_b) \, ds \quad (12)$$

$$\mathbf{f}^{\text{ext}} = \int_{\partial \Omega_a} \mathbf{N}^T \cdot \mathbf{t}_a^0 ds \quad (13)$$

In the above equations,  $\mathbf{f}^{\text{int}}$ ,  $\mathbf{f}^{\text{coh}}$ , and  $\mathbf{f}^{\text{ext}}$  are the internal, cohesive, and external forces in the system, respectively. In order to trace the equilibrium path, Eq. 9 should have zero residual:

$$\mathbf{R}(\mathbf{u}_\alpha, \lambda) = \lambda \mathbf{f}^{\text{ext}} + \mathbf{f}^{\text{coh}} - \mathbf{f}^{\text{int}} = 0 \quad (5)$$

Eq. 14 has to be solved for both  $\mathbf{u}_\alpha$  and  $\lambda$  simultaneously using an iterative non-linear solver. Nevertheless, as previously stated, an arc length method is required to simulate the response of the system when there is a reduction in the material stiffness since displacement control or load control methods alone fail to converge at the onset of global softening. Here we implemented Crisfield and Modified Crisfield-Ramm arc length methods [79]. A robust arc length method facilitates the study of load-displacement of the microstructure until a full fracture occurs.

### 3.4.3 Method verification

In order to verify the method implementation, a simple three-grain specimen (Figure 18) with normalized dimensions was modeled in ABAQUS and compared with the present method. In this case, a consistent linear cohesive law at the grain boundaries was used. A 1000 (N/m) normal traction was applied on the right edge of the specimen while the left edge was held fixed. High stiffness without softening is modeled for elements in contact to prevent material interpenetration at the grain boundaries.

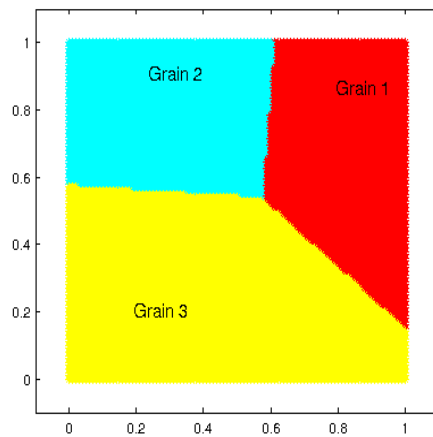


**Figure 18:** Three-grain specimen with normalized dimension

Aluminum 6061 material properties were chosen for the bulk material. Contours of  $\sigma_{xx}$  for the two solutions are depicted in Figure 19. A good agreement between the XFEM and ABAQUS results is observed. To achieve a smooth strain field in an ABAQUS solution, the nodes of the adjacent elements at the two sides of any interface have to be coinciding. This becomes an extremely burdensome task to fulfill in order to mesh more complex geometries. Nevertheless, this problem is eliminated in XFEM by implicitly modeling the interfaces. In fact, relatively accurate results could be achieved with an even fewer number of elements in the XFEM solution.

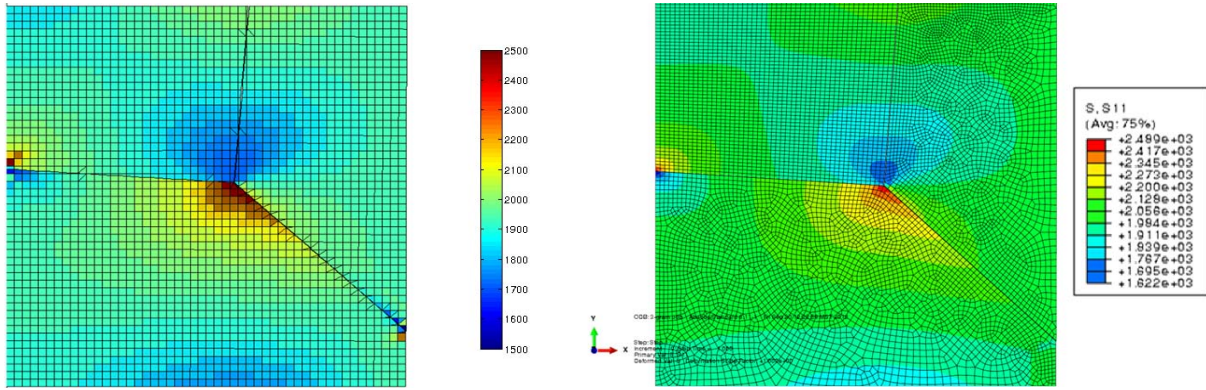


**Figure 19:** (a) XFEM solution with a 2500-element structured mesh, and (b) ABAQUS solution with a 7500-element unstructured mesh

### 3.4.4 Effect of local grain boundary characteristic on the crack growth

In this section a qualitative parametric study is performed to demonstrate the effect of different variations of grain boundary cohesive behavior on small crack growth (SCG) in polycrystalline material. As mentioned before, traction-separation laws follow the Needleman's model [82]:

$$T(\Delta) = T_0 \frac{16e^2}{9} \frac{\Delta}{\Delta_0} \exp\left(-\frac{16e^2}{9} \frac{\Delta}{\Delta_0}\right) \quad (6)$$

where  $T$  is the traction,  $\Delta$  is the separation distance, and  $\Delta_0$  is the maximum separation distance before new cracked surfaces are formed and  $T_0$  is the maximum traction in the traction-separation curve. Reference energy for interface decohesion (separation energy) is considered to be  $G = 0.85$  (J/m<sup>2</sup>) with  $T_0 = 4$  GPa and  $\Delta_0 = 4$  (Å). Here a microstructure shown in Figure 20 is simulated for three cases of different combinations of grain boundary cohesive zone models (Table 1).

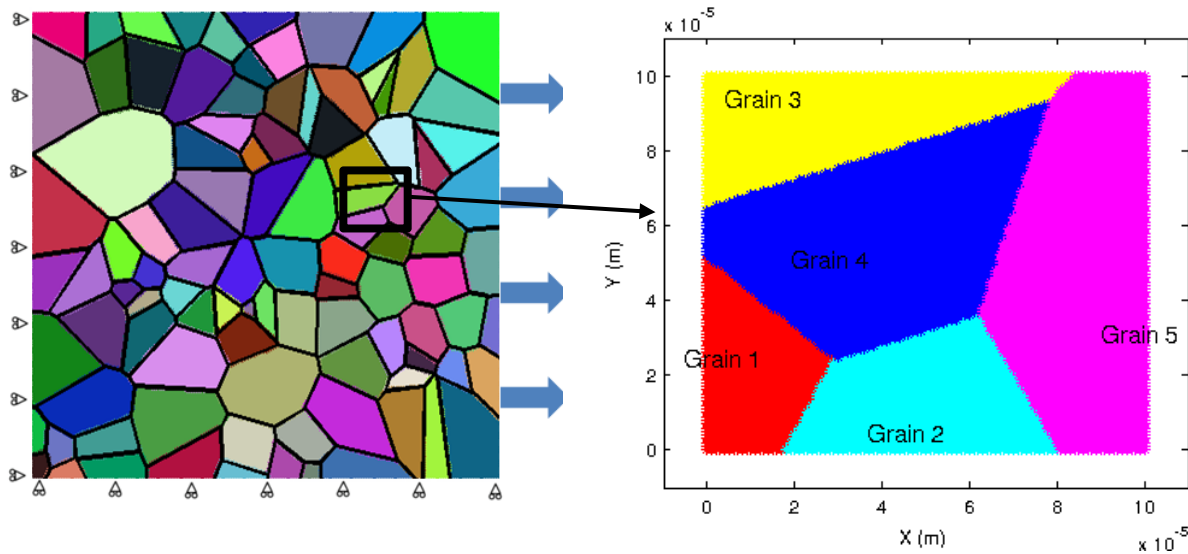


**Figure 20: Microstructure under tensile loading**

All the six different cohesive zone models (CZM) in Table 1 are considered and normalized with respect to the reference cohesive zone model (CZM 1) and depicted in Figure 21.

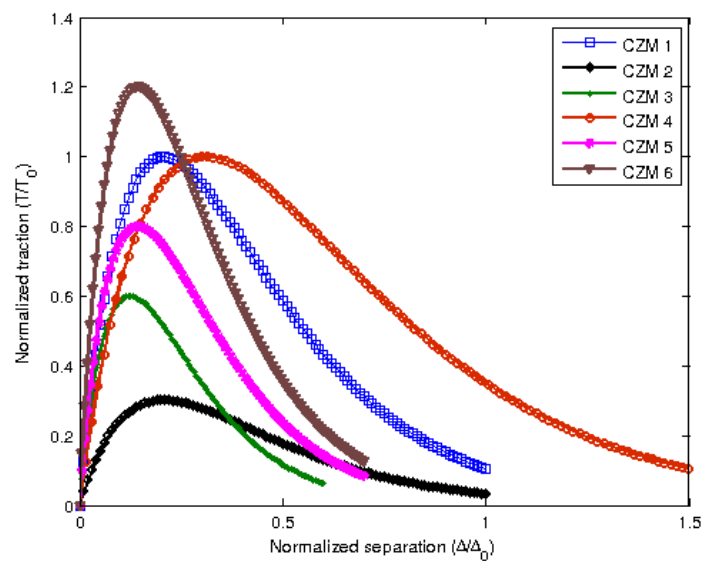


**Figure 21: Different normalized cohesive zone models**

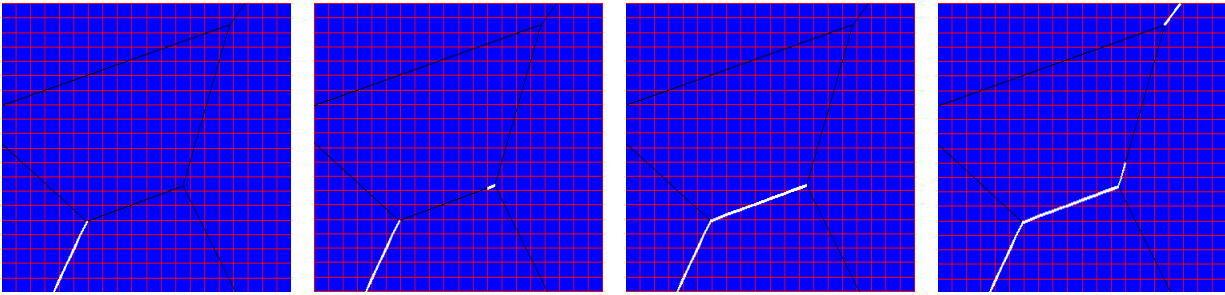
**Table 1: Cohesive law for three test cases**

Grain Boundary	GB 12	GB 14	GB 25	GB 24	GB 34	GB 35	GB 45
----------------	-------	-------	-------	-------	-------	-------	-------

Case 1	CZM 2	CZM 3	CZM 1	CZM 1	CZM 5	CZM 6	CZM 1
Case 2	CZM 2	CZM 2	CZM 2	CZM 1	CZM 6	CZM 1	CZM 1
Case 3	CZM 4	CZM 4	CZM 4	CZM 3	CZM 1	CZM 4	CZM 4

Grain boundary sliding stiffness is taken to be a high value compared to the normal stiffness. Additionally, high penalty stiffness is assumed to avoid interpenetration at grain boundaries. Because the intent here is to investigate the effect of different cohesive zone models on intergranular fracture, elastic modulus of the bulk material is taken to be very high. The fully debonded (crack) surfaces are delineated in Figure 22 by white lines. Uniform load is being applied on the right edge and the other edges are constrained.  $\lambda_n$  in Figure 22 denotes the externally applied load, non-dimensionalized by  $T_0$ , and  $\varepsilon_n$  is the average strain of the right edge. It should be noted that these values are given merely for comparison reasons and they do not represent the actual response of the microstructure.

Case 1



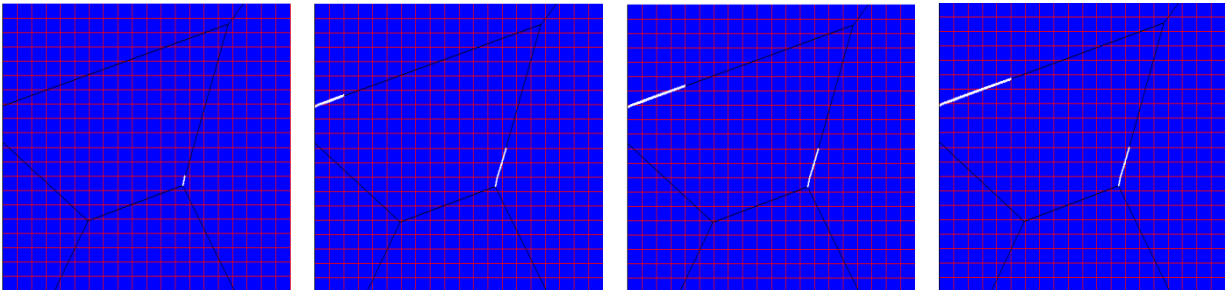
(a)  $\lambda_n=0.45$  ,  $\varepsilon_n=0.58\text{e-}4$

(b)  $\lambda_n=0.52$  ,  $\varepsilon_n=0.99\text{e-}4$

(c)  $\lambda_n=0.28$  ,  $\varepsilon_n=1.12\text{e-}4$

(d)  $\lambda_n=0.07$  ,  $\varepsilon_n=2.06\text{e-}4$

Case 2



(a)  $\lambda_n=0.24$  ,  $\varepsilon_n=0.27\text{e-}4$       (b)  $\lambda_n=0.14$  ,  $\varepsilon_n=2.46\text{e-}4$       (c)  $\lambda_n=0.07$  ,  $\varepsilon_n=2.48\text{e-}4$       (d)  $\lambda_n=0.05$  ,  $\varepsilon_n=2.49\text{e-}4$

### Case 3

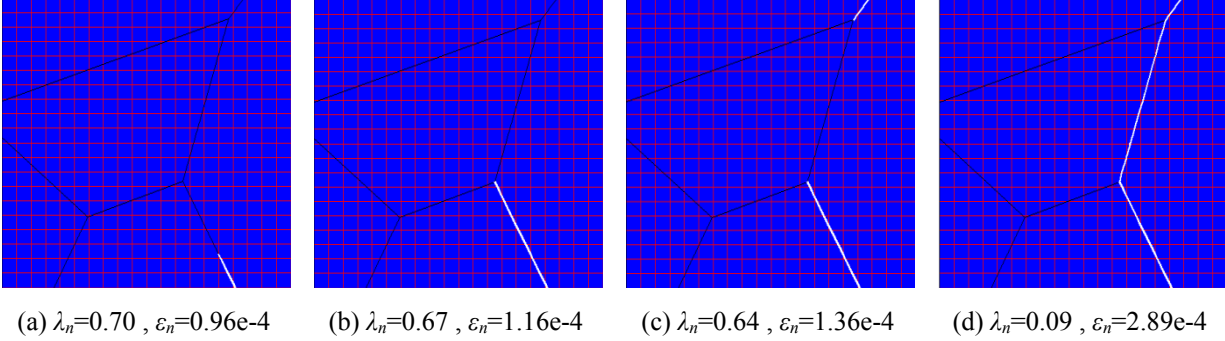


**Figure 22:** Effect of different grain boundary CZMs on small crack nucleation and growth

As it is evident from Figure 22, different grain boundary properties can yield different patterns for crack nucleation and growth in microstructure. This indicates the importance of the incorporation of each grain boundary characteristic in finite element simulations.

### 3.4.5 Crystal plasticity formulation including twinning

Incorporation of crystallographic plastic slips in the crystalline materials has been long established using rigorous phenomenological constitutive laws to capture the anisotropic stress-strain response, evolution of texture, and macroscopic behavior of the polycrystalline materials [1, 2]. Originally the crystal plasticity constitutive laws were developed for FCC material. Nevertheless, effect of deformation twinning mechanism as a mode of plastic deformation in many materials such as Ti cannot be simply neglected. In order to take into account the effect of twinning, a statistical criterion is used which is based on the volume fraction of twinned zones in the entire microstructure.

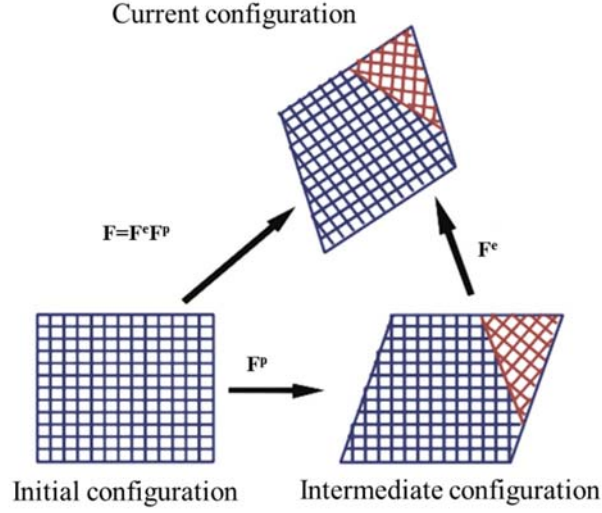


Figure 23: Multiplicative decomposition of the deformation gradient.

The crystal plasticity constitutive law used in this study is based on multiplicative decomposition (see Figure 23) of total deformation gradient where  $F = F^e F^p$ , where  $F^e$  and  $F^p$  are the elastic and plastic deformation gradients. The time rate of plastic part of the deformation gradient is calculated by

$$\dot{F} = L^p F^p \quad (36)$$

where

$$L^p = (1 - \sum_{\beta}^{N^{twin}} f^{\beta}) \sum_{\alpha}^{N^{slip}} \dot{\gamma}^{\alpha} S_{0-slip}^{\alpha} + \sum_{\beta}^{N^{twin}} \dot{f}^{\beta} \gamma^{twin} S_{0-twin}^{\beta} \quad (37)$$

is the velocity gradient of the plastic deformation,  $S_{0-slip}^{\alpha}$  and  $S_{0-twin}^{\beta}$  are the Schmid tensors for the slip system  $\alpha$  and twinning system  $\beta$ , respectively, and  $f^{\beta}$  is the volume fraction of and twinning system  $\beta$ .  $\gamma^{twin}$  is a constant shear strain associated with twinning. A phenomenological flow rule is used to calculate the rate of slip on slip system  $\alpha$  [3]

$$\dot{\gamma}^{\alpha} = \dot{\gamma}_0 \left| \frac{\tau^{\alpha}}{s^{\alpha}} \right|^{\frac{1}{m}} \text{sign}(\tau^{\alpha}) \quad (38)$$

where  $\dot{\gamma}_0$  is a reference slip rate,  $m$  is the rate sensitivity parameter, and  $\tau^{\alpha}$  and  $s^{\alpha}$  are resolved shear stress and resistance on slip system  $\alpha$ , respectively. Evolution of deformation twin volume fraction is obtained by a power-law relation

$$\dot{f}^\beta = \begin{cases} \frac{\dot{\gamma}_0}{\gamma^{twin}} \left( \frac{\tau^\beta}{s_{twin}^\beta} \right) \\ 0 \end{cases} \quad (39)$$

where  $\tau^\beta$  and  $s^\beta$  are resolved shear stress and twin resistance on twin system  $\beta$ , respectively. The evolution of the slip and twin resistance in the above formulations are updated by

$$\dot{s}^\alpha = h_{slip} (1 + C \sum_{\beta}^{N^{twin}} f^\beta) (1 - \frac{s^\alpha}{s_s^\alpha})^a \sum_k^{N^{slip}} \dot{\gamma}^k \quad (40)$$

$$\dot{s}^\beta = h_{twin} (\sum_m^{N^{twin}} f^m)^b \sum_k^{N^{twin}} \gamma^{twin} \dot{f}^k + h_{twin/slip} (\sum_{\alpha}^{N^{slip}} \gamma^\alpha)^d \sum_k^{N^{slip}} \dot{\gamma}^k \quad (41)$$

$h_{slip}$  and  $h_{twin}$  are slip and twin hardening modulus, respectively.  $C$ ,  $a$ ,  $b$  and  $d$  are hardening parameters that control the contribution of different resistance mechanism for slip, twin and twin-slip interaction. Further details on the physical phenomenology of the above formulae can be found in the literature [3].

### 3.4.6 Fatigue test

In order to estimate the effect of oxygen on fatigue life of Ti, strain controlled fatigue tests were performed on 125 mm long single edge notch tensile specimens of CP-Ti and Ti-O with an  $R$  ratio of 0.1 under displacement control method (max strain  $\sim 0.1\%$ ). The notch was machined using EDM and samples were polished. Imaging was performed using a microscope camera with a 10x magnification to identify the crack initiation and growth ahead of the notch. DIC was performed with the images captured post-deformation. Microprobe analysis was performed post deformation due to restrictions of sample size.

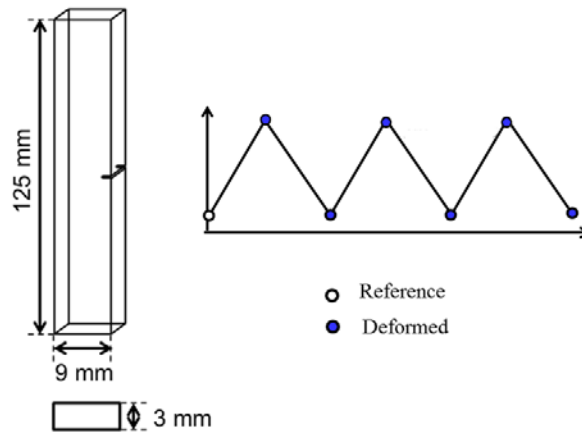




Figure 24: Single edge notch tension sample geometry used in fatigue test and DIC measurement scheme where images were captured at no load and maximum load conditions.

For the finite element simulations, crystal plasticity parameters were first calibrated using *ab-initio* calculations on dislocation motion energetics. As it was shown in the previous section, presence of oxygen reduces the slip activity by increasing the dislocation motion energy on some of the slip systems in Ti, including the dominant prismatic system. Table 1 shows how oxygen changes the maximum stacking fault energy on different slip systems in Ti which consequently leads to changes in the corresponding CRSS values.

**Table 1: Dislocation motion energy (GSFE) for CP-Ti and Ti-O**

	Maximum GSFE (mJ/m <sup>2</sup> )		
Slip System	Ti	Ti-O (20% ml oxygen content)	Ratio
Prismatic	237	303.17	1.28
Basal	278	168	0.60
Pyramidal<a>	761.21	1026.7	1.34
Pyramidal<c+a>	442	430	0.97

This can significantly contribute to the increase in the initial yield strength of Ti in presence of oxygen, which has been depicted in Figure 25 and compared with crystal plasticity FEM simulations.

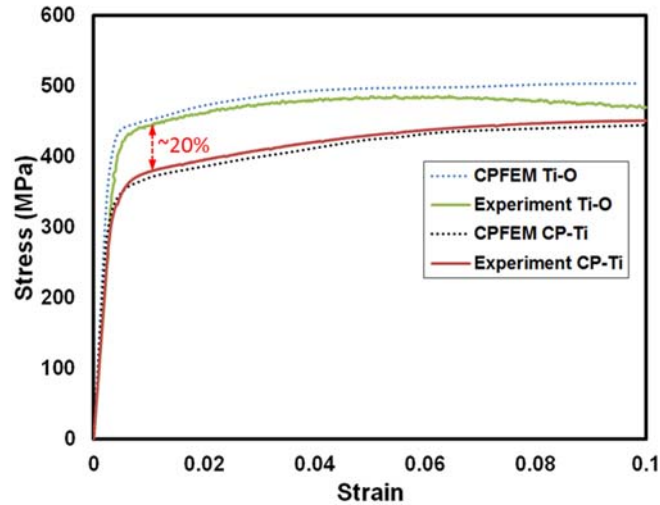


Figure 25: True stress vs. true strain curves for CP-Ti and Ti-O obtained from experiments and compared against CPFEM simulations.

On the other hand, degrading effect of oxygen on the grain boundaries makes them preferable sites for nucleation and propagation of small cracks in an intergranular fashion, which is consistent with the experimental results (Figure 26).

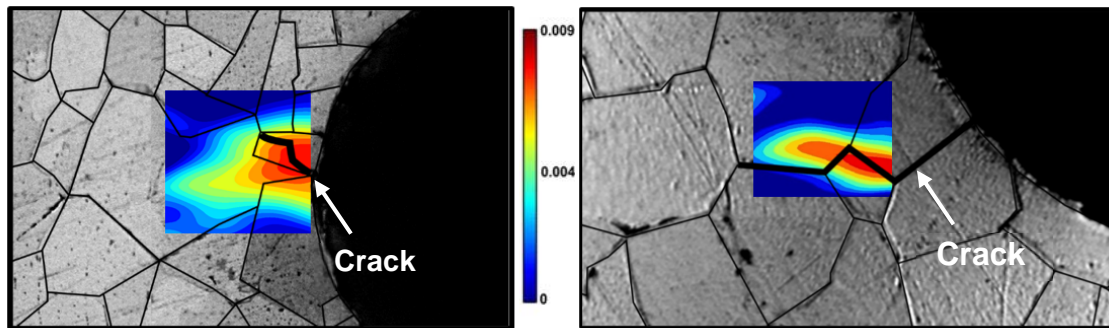


Figure 26: DIC images and underlying microstructure in CP-Ti (left) and Ti-O (right). The contours indicate magnitude of strain during fatigue testing along the loading direction.

CPFEM simulations were carried out on 2D notched samples with the calibrated parameters. In order to reduce the computational costs, the process zone was limited to a region close to the notch and the rest of the domain was considered to deform in an isotropic homogenized elasto-plastic manner (see Figure 27).

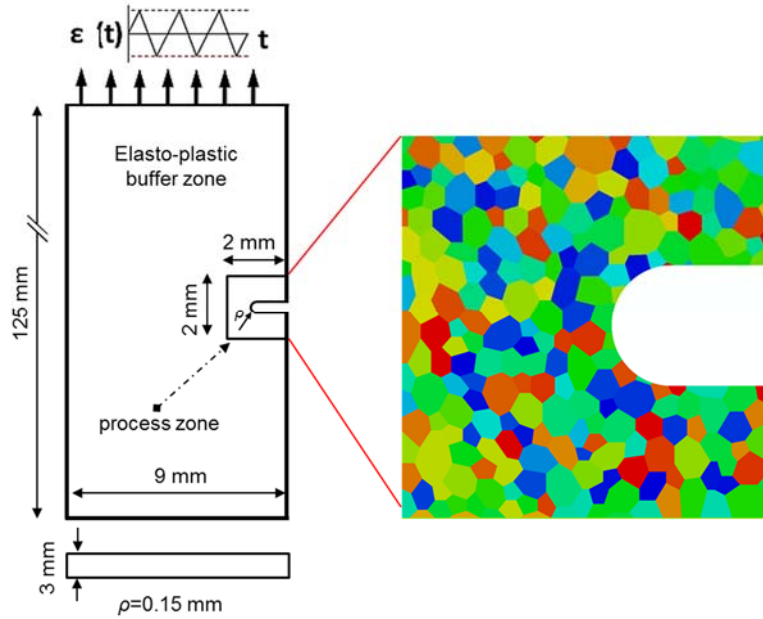


Figure 27: Computational geometry and the modeling strategy for CPFEM.

This assumption is valid since the notch stress concentration effect is dominant only within a small region ahead of notch in a microstructure-sensitive model. This robust framework can capture the complexity of a real microstructure, effects of notch size and characteristic length in the distribution of slips in the microstructure, which can be used to estimate the fatigue life of the material. The normalized total plastic shear strain contours for CP-Ti and Ti-O tests after 100 cycles were obtained using CPFEM and illustrated in Figure 28.

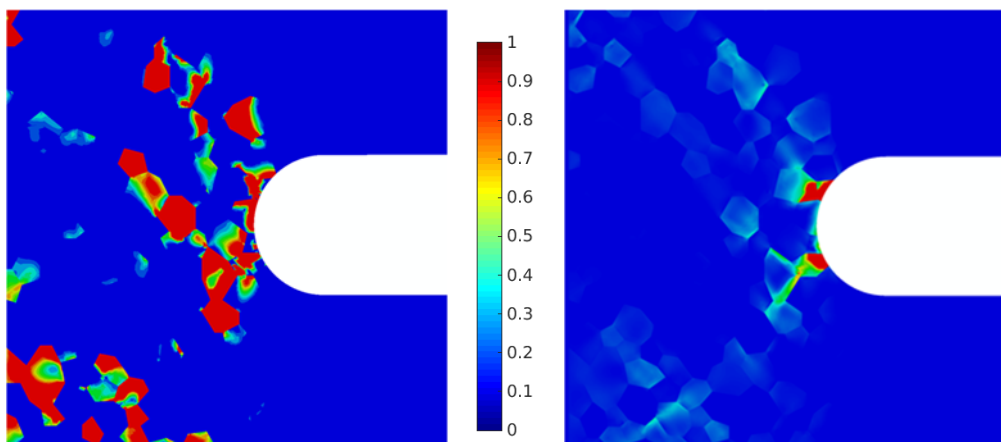


Figure 28: Normalized total plastic shear strain for CP-Ti (left) and Ti-O (right).

As clearly seen in the figure, the presence of oxygen considerably reduces the slip activity ahead of the notch and instead facilitate the grain boundary decohesion as seen previously. Grain level calculations of slips can be used to estimate the probability of small crack initiation and growth within the microstructure.

#### **4. Summary**

We have made substantial progress towards understanding the deformation mechanism by focusing on the effect of grain boundary character distributions and developing the necessary multiscale tools. Overall, we have generalized XFEM to include implicit representation of grains and grain boundaries. The new formulation can incorporate microstructure features directly based on EBSD data using level set formulations. Furthermore, an atomistic database of interactions of dislocation-impurities was developed. Using the developed database an appropriate crystal plasticity model was developed to investigate SCG in Ti alloys.

#### **References to publications of AFOSR sponsored research**

1. Bhatia, M.A., Solanki, K.N. (2013). Energetics of vacancy segregation to symmetric tilt grain boundaries in HCP materials, *Journal of Applied Physics*, 114 (24), 244309.
2. Bhatia, M.A., Zhang, X., Azarnoush, M., Lu, G., Solanki, K.N. (2015). Effects of oxygen on prismatic faults in  $\alpha$ -Ti: A combined quantum mechanics/molecular mechanics study, *Scripta Materialia*, 98, 32-35.
3. Bhatia, M.A., Azarnoush M., Adlakha I., Solanki, K.N.\* (2016). Dislocation core structure and dynamics of  $\alpha$ -Ti: A molecular static and dynamic study, *MSMSE*, (minor revision).
4. Bhatia, M. A., Solanki, K.N., (2016) Solute Effect on (10-12) Twin Boundary in Titanium: A first principle study, *Materials Research Letters*, (in review).
5. Bhatia, M.A., Adlakha, I., Solanki, K.N.\* (2016). Interactions between lattice dislocations and grain boundaries in  $\alpha$ -Ti, *Scripta Mat* (in review).
6. Solanki, K.N., Bhatia, M.A., Zhang, X., Azarnoush, M., Lu, G. (2015) Role of oxygen on mechanical properties of high temperature materials: A QM/MM study, the 2015 TMS annual meeting, Orlando, FL.

## References

- [1] C. Leyens, M. Peters, Titanium and Titanium Alloys: Fundamentals and Applications, 2003.
- [2] M.C. Brandes, M. Baughman, M.J. Mills, J.C. Williams, Materials Science and Engineering: A 551 (2012) 13–18.
- [3] H. Dong, X.Y. Li, Materials Science and Engineering: A 280 (2000) 303–310.
- [4] Z. Liu, G. Welsch, MTA 19 (1988) 1121–1125.
- [5] J. Stringer, Acta Metallurgica 8 (1960) 758–766.
- [6] A.B. Pandey, R.S. Mishra, A.G. Paradkar, Y.R. Mahajan, Acta Materialia 45 (1997) 1297–1306.
- [7] W. Luo, C. Shen, Y. Wang, Acta Materialia 55 (2007) 2579–2586.
- [8] H.H. Wu, D.R. Trinkle, Phys. Rev. Lett. 107 (2011) 45504.
- [9] J.C. Williams, A.W. Sommer, P.P. Tung, MT 3 (1972) 2979–2984.
- [10] G. Henkelman, B.P. Uberuaga, H. Jónsson, The Journal of Chemical Physics 113 (2000) 9901–9904.
- [11] Q. Zhao, R.G. Parr, The Journal of Chemical Physics 98 (1993) 543–548.
- [12] Q. Zhao, R.C. Morrison, R.G. Parr, Physical Review A 50 (1994) 2138.
- [13] G. Kresse, J. Hafner, Physical Review B 47 (1993) 558.
- [14] M.S. Daw, M.I. Baskes, Physical Review Letters 50 (1983) 1285–1288.
- [15] R.R. Zope, Y. Mishin, Phys. Rev. B 68 (2003) 24102.
- [16] X. Zhang, G. Lu, W.A. Curtin, Physical Review B 87 (2013) 54113.
- [17] A. Stukowski, Modelling Simul. Mater. Sci. Eng. 18 (2010) 15012.
- [18] V.V. Bulatov, E. Kaxiras, Phys. Rev. Lett. 78 (1997) 4221–4224.
- [19] Y.N. Osetsky, D.J. Bacon, Modelling and Simulation in Materials Science and Engineering 11 (2003) 427.
- [20] S. Plimpton, Journal of Computational Physics 117 (1995) 1–19.
- [21] P.E. Blöchl, Phys. Rev. B 50 (1994) 17953–17979.
- [22] J.P. Perdew, K. Burke, M. Ernzerhof, Phys. Rev. Lett. 78 (1997) 1396–1396.
- [23] Y. Song, Z. Guo, R. Yang, Philosophical Magazine A 82 (2002) 1345–1359.
- [24] D.M. Saylor, B.S. El Dasher, A.D. Rollett, G.S. Rohrer, Acta Materialia 52 (2004) 3649–3655.
- [25] D.M. Saylor, A. Morawiec, G.S. Rohrer, Acta Materialia 51 (2003) 3675–3686.
- [26] E.A. Holm, D.L. Olmsted, S.M. Foiles, Scripta Materialia 63 (2010) 905–908.
- [27] T. Watanabe, Materials Science and Engineering: A 176 (1994) 39–49.
- [28] A.P. Sutton, V. Vitek, Phil. Trans. R. Soc. Lond. A 309 (1983) 1–36.
- [29] W. Gui-Jin, V. Vitek, Acta Metallurgica 34 (1986) 951–960.
- [30] D. Kinderlehrer, I. Livshits, G.S. Rohrer, S. Ta’asan, P. Yu, Materials Science Forum 467–470 (2004) 1063–1068.
- [31] C.-S. Kim, A.D. Rollett, G.S. Rohrer, Scripta Materialia 54 (2006) 1005–1009.
- [32] D. Wolf, Acta Metallurgica et Materialia 38 (1990) 781–790.
- [33] G.S. Rohrer, J Mater Sci 46 (2011) 5881–5895.
- [34] K.N. Solanki, M.A. Tschopp, M.A. Bhatia, N.R. Rhodes, Metall and Mat Trans A 44 (2013) 1365–1375.
- [35] D. Brandon, B. Ralph, S. Ranganathan, M. Wald, Acta Metallurgica 12 (1964) 813–821.

- [36] R.C. Pond, *Proc. R. Soc. Lond. A* 357 (1977) 471–483.
- [37] H. Kokawa, T. Watanabe, S. Karashima, *Philosophical Magazine A* 44 (1981) 1239–1254.
- [38] R.W. Balluffi, Y. Komem, T. Schober, *Surface Science* 31 (1972) 68–103.
- [39] P.D. Bristowe, A.G. Crocker, *Philosophical Magazine A* 38 (1978) 487–502.
- [40] M.A. Rodriguez, D.M. Follstaedt, J.A. Knapp, L.N. Brewer, E.A. Holm, S.M. Foiles, K.M. Hattar, B.B. Clark, D.L. Olmsted, D.L. Medlin, *Science at the Interface: Grain Boundaries in Nanocrystalline Metals.*, Sandia National Laboratories, 2009.
- [41] P. Peralta, C. Laird, *Acta Materialia* 45 (1997) 3029–3046.
- [42] S. Plimpton, *Journal of Computational Physics* 117 (1995) 1–19.
- [43] M.A. Tschopp, K.N. Solanki, F. Gao, X. Sun, M.A. Khaleel, M.F. Horstemeyer, *Phys. Rev. B* 85 (2012) 64108.
- [44] J. Friedel, *Philosophical Magazine Series 7* 43 (1952) 153–189.
- [45] K.N. Solanki, M.A. Tschopp, M.A. Bhatia, N.R. Rhodes, *Metallurgical and Materials Transactions A* 44 (2012) 1365–1375.
- [46] R.G. Hennig, T.J. Lenosky, D.R. Trinkle, S.P. Rudin, J.W. Wilkins, *Phys. Rev. B* 78 (2008) 54121.
- [47] J. Wang, I.J. Beyerlein, *Modelling Simul. Mater. Sci. Eng.* 20 (2012) 24002.
- [48] J. Wang, I.J. Beyerlein, *Metall and Mat Trans A* 43 (2012) 3556–3569.
- [49] A. Sutton, V. Vitek, *Philosophical Transactions of the Royal Society of London. Series A, Mathematical and Physical Sciences* 309 (1983) 1–36.
- [50] E.O. Hall, *Proc. Phys. Soc. B* 64 (1951) 747.
- [51] N.J. Petch, *Progress in Metal Physics* 5 (1954) 1–52.
- [52] J.. Livingston, B. Chalmers, *Acta Metallurgica* 5 (1957) 322–327.
- [53] T.C. Lee, I.M. Robertson, H.K. Birnbaum, *Scripta Metallurgica* 23 (1989) 799–803.
- [54] W.A.T. Clark, R.H. Wagoner, Z.Y. Shen, T.C. Lee, I.M. Robertson, H.K. Birnbaum, *Scripta Metallurgica et Materialia* 26 (1992) 203–206.
- [55] Z. Shen, R.H. Wagoner, W.A.T. Clark, *Scripta Metallurgica* 20 (1986) 921–926.
- [56] Z. Shen, R.H. Wagoner, W.A.T. Clark, *Acta Metallurgica* 36 (1988) 3231–3242.
- [57] L. Wang, Y. Yang, P. Eisenlohr, T.R. Bieler, M.A. Crimp, D.E. Mason, *Metall and Mat Trans A* 41 (2010) 421–430.
- [58] J. Luster, M.A. Morris, *MMTA* 26 (1995) 1745–1756.
- [59] D. Saraev, S. Schmauder, *Phys. Stat. Sol. (B)* 240 (2003) 81–90.
- [60] Y. Cheng, M. Mrovec, P. Gumbsch, *Philosophical Magazine* 88 (2008) 547–560.
- [61] M.P. Dewald, W.A. Curtin, *Philosophical Magazine* 87 (2007) 4615–4641.
- [62] M.D. Sangid, T. Ezaz, H. Sehitoglu, I.M. Robertson, *Acta Materialia* 59 (2011) 283–296.
- [63] M. Yuasa, K. Masunaga, M. Mabuchi, Y. Chino, *Philosophical Magazine* 94 (2014) 285–305.
- [64] J. Kacher, B.P. Eftink, B. Cui, I.M. Robertson, *Current Opinion in Solid State and Materials Science* 18 (2014) 227–243.
- [65] M.P. Dewald, W.A. Curtin, *Modelling Simul. Mater. Sci. Eng.* 15 (2007) S193.
- [66] C.L. Kelchner, S.J. Plimpton, J.C. Hamilton, *Physical Review B* 58 (1998) 11085.
- [67] C.A. Schuh, *Materials Today* 9 (2006) 32–40.
- [68] S.R. Kalidindi, S.J. Vachhani, *Current Opinion in Solid State and Materials Science* 18 (2014) 196–204.
- [69] T. Ohmura, A. m. Minor, E. a. Stach, J. w. Morris, *Journal of Materials Research* 19 (2004) 3626–3632.

- [70] J. Gemperlová, A. Jacques, A. Gemperle, N. Zárubová, in: Symposium Y – Influences of Interface & Dislocation Behavior on Microstructure Evolution, 2000.
- [71] M. g. Wang, A. h. w. Ngan, Journal of Materials Research 19 (2004) 2478–2486.
- [72] T. b. Britton, D. Randman, A. j. Wilkinson, Journal of Materials Research 24 (2009) 607–615.
- [73] Y.M. Hu, W. Floer, U. Krupp, H.-J. Christ, Materials Science and Engineering: A 278 (2000) 170–180.
- [74] S. Kobayashi, T. Inomata, H. Kobayashi, S. Tsurekawa, T. Watanabe, Journal of Materials Science 43 (2008) 3792–3799.
- [75] L.C. Lim, T. Watanabe, Acta Metallurgica et Materialia 38 (1990) 2507–2516.
- [76] T. Watanabe, S. Tsurekawa, Acta Materialia 47 (1999) 4171–4185.
- [77] T. Belytschko, T. Black, International Journal for Numerical Methods in Engineering 45 (1999) 601–620.
- [78] J. Qian, S. Li, J. Eng. Mater. Technol. 133 (2010) 011010–011010.
- [79] M. Fafard, B. Massicotte, Computers & Structures 46 (1993) 603–615.
- [80] T.-P. Fries, A. Byfut, A. Alizada, K.W. Cheng, A. Schröder, Int. J. Numer. Meth. Engng. 86 (2011) 404–430.

# AFOSR Deliverables Submission Survey

Response ID:6571 Data

1.

## 1. Report Type

Final Report

## Primary Contact E-mail

Contact email if there is a problem with the report.

knsolank@asu.edu

## Primary Contact Phone Number

Contact phone number if there is a problem with the report

480-965-1869

## Organization / Institution name

Arizona State University

## Grant/Contract Title

The full title of the funded effort.

Hierarchically-driven approach for quantifying fatigue crack initiation and short crack growth behavior in aerospace materials

## Grant/Contract Number

AFOSR assigned control number. It must begin with "FA9550" or "F49620" or "FA2386".

FA9550-13-1-0144

## Principal Investigator Name

The full name of the principal investigator on the grant or contract.

Kiran Solanki

## Program Manager

The AFOSR Program Manager currently assigned to the award

James Fillerup

## Reporting Period Start Date

03/15/2013

## Reporting Period End Date

03/14/2016

## Abstract

Here, we present a hierarchical form of multiscale modeling to understand fundamental issues of deformation in Ti. This report presents our effort in the following areas,

1. Effects of oxygen on prismatic faults in  $\alpha$ -Ti: A combined quantum mechanics/molecular mechanics study
2. Nano-indentation and slip transfer (critical in understanding crack initiation)
3. An extended-finite element framework (XFEM) to study SCG mechanisms
4. Atomistic methods to develop a grain and twin boundaries database in  $\alpha$ -Ti to quantify and develop
  - a. a crack initiation model,
  - b. the necessary cohesive zone models for interfaces and single crystals, and
  - c. a crystal plasticity model

Fundamental to the development of a hierarchical atomistic-continuum methodology for SCG is the development of appropriate crack initiation models, cohesive zone properties, crystal plasticity models, and the microstructure based finite element framework, i.e., in this case, we are using an XFEM. Overall, we

DISTRIBUTION A: Distribution approved for public release.



have generalized XFEM to include implicit representation of grains and grain boundaries. The new formulation can incorporate microstructure features directly based on EBSD data using level set formulations. Furthermore, an atomistic database of interactions of dislocation-impurities was developed. Using the developed database an appropriate crystal plasticity model was developed to investigate SCG in Ti alloys.

### **Distribution Statement**

This is block 12 on the SF298 form.

Distribution A - Approved for Public Release

### **Explanation for Distribution Statement**

If this is not approved for public release, please provide a short explanation. E.g., contains proprietary information.

### **SF298 Form**

Please attach your SF298 form. A blank SF298 can be found [here](#). Please do not password protect or secure the PDF. The maximum file size for an SF298 is 50MB.

[SF298 FA9550-13-1-0144.pdf](#)

**Upload the Report Document. File must be a PDF. Please do not password protect or secure the PDF. The maximum file size for the Report Document is 50MB.**

[FA9550-3-1-0144 Solanki Final.pdf](#)

**Upload a Report Document, if any. The maximum file size for the Report Document is 50MB.**

### **Archival Publications (published) during reporting period:**

1. Bhatia, M.A., Solanki, K.N. (2013). Energetics of vacancy segregation to symmetric tilt grain boundaries in HCP materials, Journal of Applied Physics, 114 (24), 244309.
2. Bhatia, M.A., Zhang, X., Azarnoush, M., Lu, G., Solanki, K.N. (2015). Effects of oxygen on prismatic faults in  $\alpha$ -Ti: A combined quantum mechanics/molecular mechanics study, Scripta Materialia, 98, 32-35.
3. Bhatia, M.A., Azarnoush M., Adlakha I., Solanki, K.N.\* (2016). Dislocation core structure and dynamics of  $\alpha$ -Ti: A molecular static and dynamic study, MSMSE, (minor revision).
4. Bhatia, M. A., Solanki, K.N., (2016) Solute Effect on (10-12) Twin Boundary in Titanium: A first principle study, Materials Research Letters, (in review).
5. Bhatia, M.A., Adlakha, I., Solanki, K.N.\* (2016). Interactions between lattice dislocations and grain boundaries in  $\alpha$ -Ti, Scripta Mat (in review).
6. Solanki, K.N., Bhatia, M.A., Zhang, X., Azarnoush, M., Lu, G. (2015) Role of oxygen on mechanical properties of high temperature materials: A QM/MM study, the 2015 TMS annual meeting, Orlando, FL.

### **2. New discoveries, inventions, or patent disclosures:**

**Do you have any discoveries, inventions, or patent disclosures to report for this period?**

No

**Please describe and include any notable dates**

**Do you plan to pursue a claim for personal or organizational intellectual property?**

**Changes in research objectives (if any):**

None

**Change in AFOSR Program Manager, if any:**

Program manager changed from David Stargel to James Fillerup

**Extensions granted or milestones slipped, if any:**

No

**AFOSR LRIR Number**

**LRIR Title**

**Reporting Period**

**Laboratory Task Manager**

DISTRIBUTION A: Distribution approved for public release.

**Program Officer**

**Research Objectives**

**Technical Summary**

**Funding Summary by Cost Category (by FY, \$K)**

	Starting FY	FY+1	FY+2
Salary			
Equipment/Facilities			
Supplies			
Total			

**Report Document**

**Report Document - Text Analysis**

**Report Document - Text Analysis**

**Appendix Documents**

**2. Thank You**

**E-mail user**

Jul 22, 2016 10:57:04 Success: Email Sent to: knsolank@asu.edu